This is the Pre-Published Version.
The following publication Liu, K., Liang, Q., Qin, M., Shen, D., Yin, H., Ren, Z., Zhang, Y., Zhang, H., Fong, P. W. K., Wu, Z., Huang, J., Hao, J., Zheng, Z., So, S. K., Lee, C.-S., Lu, X., & Li, G. (2020). Zwitterionic-Surfactant-Assisted Room-Temperature Coating of Efficient Perovskite Solar Cells. Joule, 4(11), 2404-2425 is available at https://doi.org/10.1016/j.joule.2020.09.011.

Joule

Zwitterionic Surfactant Assisted Room Temperature Coating of Efficient Perovskite Solar Cells

--Manuscript Draft--

Manuscript Number:	JOULE-D-20-00524R3
Full Title:	Zwitterionic Surfactant Assisted Room Temperature Coating of Efficient Perovskite Solar Cells
Article Type:	Research Article
Keywords:	Zwitterionic surfactant; Meniscus coating; Perovskite solar cells; Crystallization kinetics; Defect passivation; Room-temperature process
Corresponding Author:	Gang Li HONG KONG
First Author:	Kuan Liu
Order of Authors:	Kuan Liu
	Qiong Liang
	Minchao Qin
	Dong Shen
	Hang Yin
	Zhiwei Ren
	Yaokang Zhang
	Hengkai Zhang
	Patrick W. K. Fong
	Zehan Wu
	Jiaming Huang
	Jianhua Hao
	Zijian Zheng
	Shu Kong So
	Chun-Sing Lee
	Xinhui Lu
	Gang Li
Abstract:	With amazing progress in the state-of-the-art perovskite solar cells (PSCs) fabricated by laboratory-scale spin-coating methods, upscaling the PSCs via printing friendly techniques is becoming more and more important towards the future deployment of large-scale and stable perovskite modules. Here, we demonstrate the room-temperature meniscus coating of high-quality perovskite films incorporated with a multifunctional sulfobetaine based zwitterionic surfactant. Systematic in-situ studies uncover the perovskite crystallization pathway and emphasize the surfactant's synergistic role in film construction, crystallization kinetics modulation, defect passivation, and moisture barrier protection. This strategy is applicable across perovskite compositions and device architectures with the enhanced power conversion efficiencies up to 22%. Upscaling the device area to 0.8 cm2 has negligible deterioration in the performance. This represents one of the highest records for the upscaling coated PSCs, not limited in room-temperature coated PSCs. In addition, this approach significantly improves the stability of perovskite films and devices under different aging conditions.

Powered by Editorial Manager® and ProduXion Manager® from Aries Systems Corporation
© 2020. This manuscript version is made available under the CC-BY-NC-ND 4.0 license http://creativecommons.org/licenses/by-nc-nd/4.0/

Opposed Reviewers:	
Suggested Reviewers:	Nam-Gyu Park, Dr. Professor, Sungkyunkwan University npark@skku.edu
	Jinsong Huang, Dr. Professor, University of North Carolina at Chapel Hill jhuang@unc.edu
	Kai Zhu, Dr. Senior Scientist, National Renewable Energy Laboratory kai.zhu@nrel.gov
	Francesca Brunetti, Dr. Associate Professor, University of Rome Tor Vergata francesca.brunetti@uniroma2.it
	Jingbi You, Dr. Professor, Institute of Semiconductors, Chinese Academy of Sciences jyou@semi.ac.cn
	Feng Gao, Dr. Professor, Linköping University feng.gao@liu.se
	Qingbo Meng, Dr. Professor, Director of Center of Clear Energy, Institute of Physics, Chinese Academy of Sciences qbmeng@iphy.ac.cn

Powered by Editorial Manager® and ProduXion Manager® from Aries Systems Corporation

Graphical Abstract

Click here to access/download;Graphical Abstract;Graphical Abstract.tif

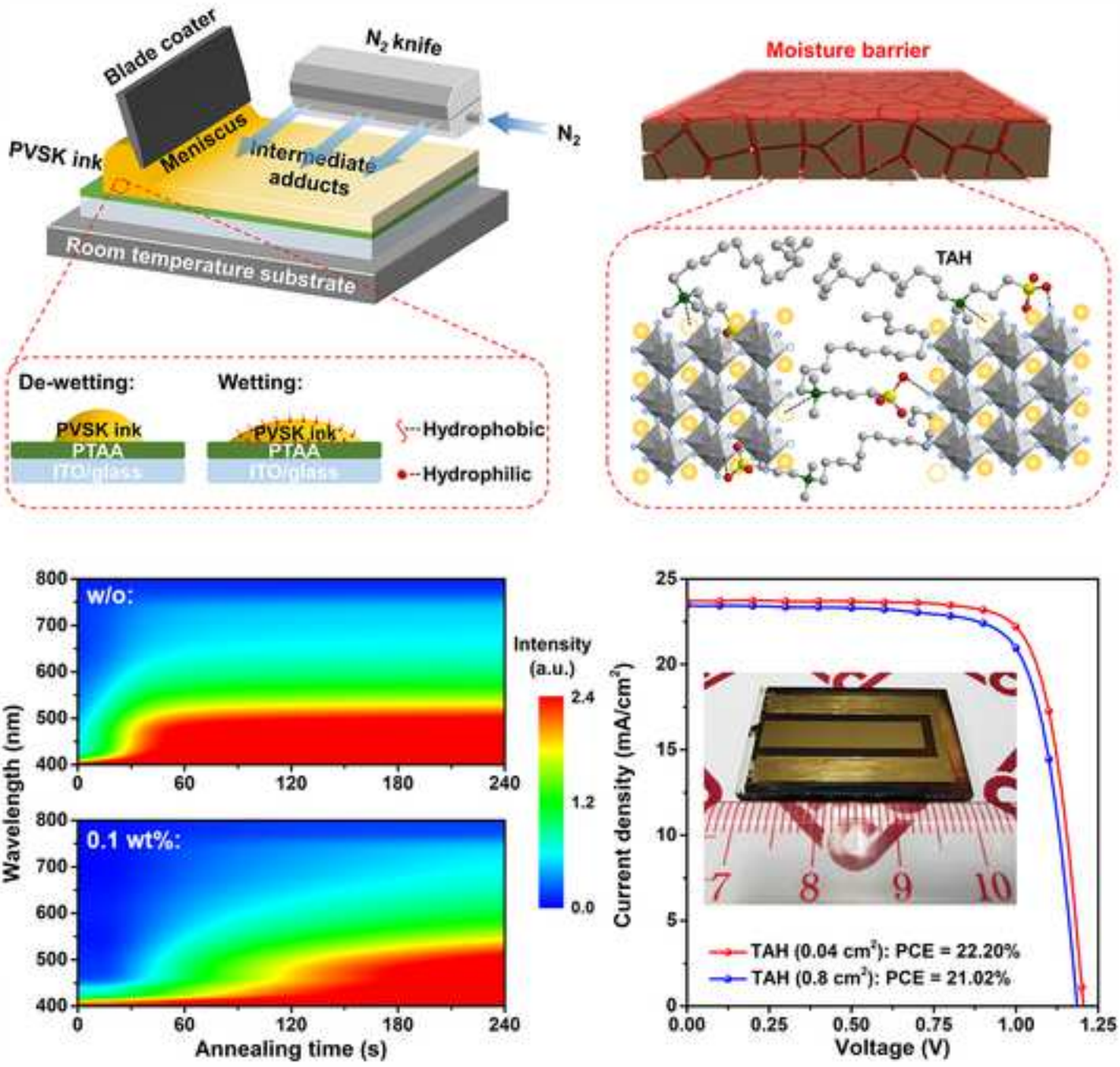

Manuscript Click here to view linked References

Zwitterionic Surfactant Assisted Room Temperature Coating of Efficient Perovskite Solar Cells

Kuan Liu,[1] Qiong Liang,[1,7] Minchao Qin,[2] Dong Shen,[3] Hang Yin,[4] Zhiwei Ren,[1,7] Yaokang Zhang,[5] Hengkai Zhang,[1,7] Patrick W. K. Fong,[1] Zehan Wu,[6] Jiaming Huang,[1,7] Jianhua Hao,[6] Zijian Zheng,[5] Shu Kong So,[4] Chun-Sing Lee,[3] Xinhui Lu,[2,*] and Gang Li[1,7,8,*]

[1]Department of Electronic and Information Engineering, Research Institute for Smart Energy (RISE), The Hong Kong Polytechnic University, Hung Hom, Kowloon, Hong Kong, China

[2]Department of Physics, The Chinese University of Hong Kong, New Territories, Hong Kong, China

[3]Center of Super-Diamond and Advanced Films (COSDAF) and Department of Chemistry, City University of Hong Kong, Kowloon, Hong Kong, China

[4]Department of Physics and Institute of Advanced Materials, Hong Kong Baptist University, Kowloon, Hong Kong, China

[5]Laboratory for Advanced Interfacial Materials and Devices, Research Centre for Smart Wearable Technology, Institute of Textiles and Clothing, The Hong Kong Polytechnic University, Hung Hom, Kowloon, Hong Kong, China

[6]Department of Applied Physics, The Hong Kong Polytechnic University, Hung Hom, Kowloon, Hong Kong, China

[7]The Hong Kong Polytechnic University Shenzhen Research Institute, Shenzhen 518057, China

[8]Lead Contact

*Correspondence: xhlu@phy.cuhk.edu.hk (X. L.), gang.w.li@polyu.edu.hk (G. L.)

SUMMARY

With amazing progress in the state-of-the-art perovskite solar cells (PSCs) fabricated by laboratory-scale spin-coating methods, upscaling the PSCs via printing friendly techniques is becoming more and more important towards the future deployment of large-scale and stable perovskite modules. Here, we demonstrate the room-temperature meniscus coating of high-quality perovskite films incorporated with a multifunctional sulfobetaine based zwitterionic surfactant. Systematic in-situ studies uncover the perovskite crystallization pathway and emphasize the surfactant's synergistic role in film construction, crystallization kinetics modulation, defect passivation, and moisture barrier protection. This strategy is applicable across perovskite compositions and device architectures with the enhanced power conversion efficiencies up to 22%. Upscaling the device area to 0.8 cm^2 has negligible deterioration in the performance. This represents one of the highest records for the upscaling coated PSCs, not limited in room-temperature coated PSCs. In addition, this approach significantly improves the stability of perovskite films and devices under different aging conditions.

INTRODUCTION

Over the past decade, organic-inorganic hybrid perovskite (OIHP) materials (such as methylammonium lead halides $MAPbX_3$, where X = I, Br, and Cl) have attracted increasing attention in the photovoltaic research community due to their outstanding and tunable electronic and optical properties, such as tunable energy levels through compositional engineering, ambipolar charge transport with long diffusion length (> 1 μm) and lifetime, excellent light absorption coefficient (≈ 10^5 cm^{-1}), and high defects tolerance.[1-3] The performance of laboratory-scale perovskite solar cells (PSCs) have made tremendous strides, reaching a certified power conversion efficiency (PCE) up to 25.2%.[4] Superior to other high-efficiency photovoltaic materials such as silicon and gallium arsenide (GaAs), perovskite polycrystalline films can be deposited in facile solution process, which is in favor of high-throughput and low-cost printing techniques for scale-up manufacture of PSCs.[5-9]

Although very promising, most of the reported high-efficiency PSCs are fabricated by spin-coating methods so far, especially by one-step spin-coating associated with antisolvent drop-casting to precipitate intermediate phase of perovskite complex.[10-12] However, this deposition technique is difficult to prepare uniform and high-quality perovskite films in relatively large area, and it cannot be compatible with industrial manufacture in the coming future.[13-15] In order to address this issue, scalable deposition techniques have recently attracted huge interests from the commercialized point of view. Many efforts have been devoted to printing techniques of perovskite photovoltaic films into larger area, including spray-coating,[16,17] slot-die coating,[18,19] doctor-blade coating,[20,21] and so on. Blade coating, also known as knife or bar coating, is a simple, cost-efficient, and roll-to-roll compatible meniscus coating technique for optoelectronic devices fabrication. Meanwhile, in order to control the drying dynamics of perovskite ink, hot-casting,[22,23] vacuum-flashing[24,25] as well as gas-quenching post-

treatments[26,27] have also been involved to replace the conventional antisolvent drop-casting. Phase transition pathways from the disordered perovskite precursor to polycrystalline perovskite thin films throughout the ink drying process have been well investigated and gleaned into the role of fluid dynamics in meniscus coating techniques.[23,28-31] Until now, PCEs of the blade-coated PSCs have rapidly climbed up to 21% for small-area devices (~0.1 cm^2), ~20% for 1.0 cm^2 devices and 16.4% for large perovskite modules (63.7 cm^2).[27,32,33] However, these results still lag behind the performance of small-area PSCs deposited by spin-coating.

Additive engineering in perovskite precursors has been well established in spin-coated PSCs.[6,12,34-37] However, coating friendly multifunctional additives special designed for scalable deposition of perovskite films towards higher performance PSCs are still lack of detailed investigation. It's a significant challenge to coat uniform and fully covered perovskite films on hydrophobic hole transport layer (HTL), such as poly[bis(4-phenyl)(2,4,6-trimethylphenyl)amine (PTAA), because of the non-wetting surface towards perovskite precursor solution (normally in polar solvent, e.g., DMF, DMSO).[38] The hydrophobic nature of PTAA HTL reduces the adhesion of perovskite ink, inducing severe shrink and pin-hole issue of the blade-coated perovskite films. In printing industry, surfactants with long alkyl chains are important additives to fine tune the surface energy of printing ink for high-quality printed films. This concept is also expanded to the printed electronics research to improve the coverage and quality of electronic films. Very recently, blade coating of the perovskite ink containing very small amount of surfactants (dozens of ppm) on a pre-heated substrate ($\geq$ 140°C) has been demonstrated to be an efficient and high-throughput deposition technology for high-quality perovskite films in large area, representing a breakthrough in the field.[39] However, most of the high-performance blade-coated PSCs involve with high temperature hot-casting post-treatment, which hinders their applications

particularly in flexible photovoltaic modules. The evaluated processing temperature leads to simultaneous fast solvent evaporation and crystal growth, which makes detailed perovskite crystallization study intractable, and process control harder. Perovskite wet films in high-temperature coating always suffer from inherent Bénard–Marangoni convection, thus yields inhomogeneous films with island microstructures.[40] In our opinion, room-temperature (RT) coating of large-area and high-quality perovskite films incorporated with multifunctional surfactants in a well-controlled manner is more desirable for the future PSCs manufacture.

In this study, we demonstrate the RT meniscus coating of high-quality perovskite photovoltaic films incorporated with a multifunctional sulfobetaine based zwitterionic surfactant, tetradecyldimethyl(3-sulfopropyl)ammonium hydroxide inner salt (TAH) (Figure S1). Besides hydrophobic (water-fear) and hydrophilic (water-friend) terminal groups, zwitterionic surfactants also carry both positive and negative charged functionalized groups connected with covalent bond. Their unique characteristics enable them to distinguish from other common organic additives and display special performance in large-scale coating.[41] We in-situ investigate the nucleation kinetics of intermediate complex and its transition to the perovskite during the ink drying and annealing process respectively using the time-resolved X-ray scattering and UV-vis absorption technologies. The coating friendly TAH not only helps to improve the adhesion of perovskite ink to the underlying hydrophobic transport layer, thus constructs a compact and smooth perovskite film with full coverage even on RT substrate, but also finely modulates the perovskite crystallization kinetics, inducing better crystallinity and dominant out-of-plane orientation. Moreover, functionalized zwitterionic moieties have strong capability to passivate the positive and negative charged defects at perovskite surface and grain boundaries (GBs) at the same time.[42,43] This strategy can be applied across perovskite compositions and device architectures with

the enhanced power conversion efficiencies (PCEs) up to 22%, for both the inverted structure $MAPbI_3$ based and conventional structure mixed triple-cation (CsFAMA) PSCs, with significant open-circuit voltage (V_{OC}) enhancement. Upscaling the active area to 0.8 cm^2 still maintains a superior efficiency over 21%. In addition, during the perovskite formation process, TAH has been shown to self-assemble at perovskite surface, especially upper surface, with hydrophobic long tails pointing outside and spontaneously forms a moisture barrier with alkyl chains intertwining. This approach significantly enhances the stability of both perovskite films and devices under the conditions of moisture stress (60% RH), high temperature stress (80°C), or continuous illumination in the ambient atmosphere.

RESULTS AND DISCUSSION

Perovskite Film Deposition and Morphology

The RT meniscus-guided blade coating technique used in this study is illustrated in Figure 1A. The perovskite precursor solution was swiped linearly by a film applicator, resulting in a wet perovskite film on the PTAA-coated indium tin oxide (ITO) substrate. The perovskite precursor solution with highly disordered ions requires additional energy to re-orientate and freezes their motion, assembling them into highly ordered crystal lattice. Thus, the formation of an intermediate adduct with less-disordered state in lower entropy can facilitate its crystallization into superior feature. In this study, enlightened by the intermediate protocol, we separated the precursor film deposition from subsequent thermal annealing in a well-controlled manner, thus allowing a RT process. The as-prepared perovskite wet film was subsequently quenched by a laminar nitrogen knife in the direction parallel to the substrate. Functionally similar to the conventional antisolvent drop-casting in spin-coating technique, this nitrogen quenching post-treatment induces instant super-saturation of precursor solution and

facilitates fast nucleation of the ordered perovskite intermediate adducts (Figure S2), which helps to trigger the formation of ultra-smooth perovskite film in large area after proper thermal annealing.[26,44,45] Figure 1C shows the photographs of the blade-coated perovskite films with different amount of TAH on PTAA coated ITO substrate after thermal annealing. De-wetting problem of perovskite ink on PTAA layer prevents the deposition of high-quality perovskite films with uniform and pinhole-free grains in the inverted p-i-n structured PSCs. In our study, the pristine perovskite ink first spreads over the substrate by the film applicator, but shrinks quickly during the quenching process, leaving partially uncovered perovskite film after annealing. The De-wetting problem can be solved when small amount (e.g. 0.1 wt%) of TAH surfactant is incorporated into the perovskite ink. The severe shrink phenomenon is eliminated during the drying process of TAH based perovskite wet film and the perovskite film displays almost 100% coverage after thermal annealing.

To better understand this process, we measured the contact angles of the corresponding perovskite droplets on PTAA coated ITO substrate, as shown in Figure 1D. The pristine perovskite droplet shows relatively large contact angle of 41.0° on PTAA layer. The contact angles are monotonically reduced when small amount of TAH is incorporated into the perovskite ink (from 0 to 0.1 wt%). The droplet containing 0.1 wt% TAH displays excellent wetting contact on PTAA with the contact angle of 19.8°. Due to its amphipathic nature, TAH provides strong capability to fine-tune the surface energy of perovskite ink and improves its adhesion to the underlying hydrophobic substrate. According to the relationship between the free energy required for heterogenous and homogenous nucleation:[46,47]

$$G_{\text{Heterogeneous}} = G_{\text{Homogeneous}} * \frac{(2+\cos\theta)(1-\cos\theta)^2}{4} \qquad \text{(Equation 1)}$$

where θ is the contact angle on the solid/liquid interface. The wetting contact of TAH based perovskite ink on PTAA results in a lower energy barrier for the formation of heterogeneous nucleation, which

benefits the formation of uniform and high-quality perovskite films with full coverage. Figure S3 shows the top-view scanning electron microscopy (SEM) images of the annealed $MAPbI_3$ based perovskite films incorporated with different amount of TAH. In the pristine perovskite, large number of pinholes can be observed at GBs, mainly due to the de-wetting problem and severe shrink of perovskite wet film during the ink drying process. On the contrary, the ink incorporated with 0.05 and 0.1 wt% TAH significantly suppresses the formation of pinhole and constructs a compact perovskite film with dense and uniform grain. We also performed cross-sectional SEM combined with energy-dispersive X-ray spectroscopy (EDX) in the pristine and TAH incorporated perovskite films which were blade-coated on PTAA/ITO substrates (Figure S4). Both perovskite films show similar thickness of ~400 nm. While, compared with the pristine film, TAH based perovskite film displays much improved physical contact with closer adhesion to the underlying PTAA/ITO substrate, which likely indicates that TAH modifies the perovskite ink/PTAA interface and improves the affinity to the underlying hydrophobic transport layer. According to the cross-sectional EDX mapping, stronger intensity of S Ka1 signal derived from TAH was clearly detected at perovskite upper surface, and the intensity decreased into the bulk.

In order to investigate TAH distribution in the bulk perovskite more precisely, we further conducted time-of-flight secondary ion mass spectrometry (ToF-SIMS) (Figure 1E). Uniform signal of PbI^- throughout the whole thickness represented the bulk perovskite. A strong signal of SO_3^- derived from TAH was detected at perovskite upper surface, which became two order of magnitude lower at ~50 nm into the bulk (~35 s sputtering time). While, deeper into the perovskite, a moderate amount of TAH was observed close to PVSK/ITO interface, which was still much lower than that at upper surface of perovskite. According to the cross-sectional EDX and ToF-SIMS results, we can conclude that TAH

prefers to self-assemble at perovskite surface, especially at upper surface due to its amphipathic nature, which spontaneously forms a moisture barrier and facilitates inner encapsulation (Figure 1B). We further measured the roughness of blade-coated perovskite films on PTAA layer using atomic force microscopy (AFM), as shown in Figure S5. The root mean square roughness (R_q) in the pristine perovskite is calculated to be 26.8 nm (area of 3 μm × 3 μm). With the incorporation of TAH surfactant from 0 to 0.1 wt%, the blade-coated perovskite becomes much smoother and pin-hole free, with reduced R_q of 18.4 nm for 0.05 wt% and 16.3 nm for 0.1 wt% TAH, which is also coincident well with the cross-sectional SEM images. TAH based perovskites also display slightly stronger UV-vis absorption (Figure S6A), which is mainly attributed to the improved coverage and quality of perovskite films. While, TAH additive does not affect the bandgap of respective perovskite films. Both the pristine and TAH based perovskite have almost identical bandgap of 1.59 eV (Figure S6B).

Perovskite Crystallization and Orientation

X-ray diffraction (XRD) measurement was performed to investigate the significant role of TAH in perovskite crystallization and grain orientation. We first isolated the intermediate phase and measured the XRD patterns of the as-cast perovskite films before thermal annealing (Figure S7). For the pristine perovskite, three main peaks located at 2θ = 6.52°, 7.18° and 9.19° can be assigned to the $(MA)_2Pb_3I_8{\cdot}2DMSO$ intermediate phase, and one peak located at 14.08° represents the tetragonal $MAPbI_3$ phase.[10,48] In comparison, the as-cast TAH based perovskite film displays a new diffraction peak located at 9.48°, but the signal of tetragonal perovskite is missing. The new peak does not belong to any known intermediate solvate.[49,50] Thus, we speculate that MAI-PbI_2-TAH as a possible intermediate phase is also precipitated during the ink drying process. This result suggests that besides

DMSO, TAH also induces extra coordination with perovskite precursors and retards the unfavored quick formation of perovskite at the early stage, which is coincident well with the film color in the as-cast perovskite (Figure S2).

In order to gain further insights into the nucleation kinetics with the incorporation of TAH, synchrotron-based in-situ grazing-incidence wide-angle X-ray scattering (GIWAXS) measurements were performed throughout the drying process of the perovskite ink with different concentrations of TAH.[51] Two-dimensional (2D) GIWAXS patterns were measured at 1 s per frame and the data collection lasted for 100 s until the scattering patterns were nearly unchanged, as shown in Figure S8. The corresponding intensity profiles and false-color intensity maps versus q and frame numbers are summarized in Figure 2A and 2B, respectively. For the pristine perovskite, a scattering halo centered at $q \approx 0.4$ Å^{-1} originates from the perovskite precursor solution at the early stage, and gradually shifts to higher q due to the removal of DMF molecules.[29,49] After ~21 s of drying, the scattering ring of precursor solution disappears, followed by the presence of a few sharp scattering peaks located at q = 0.468, 0.515, and 0.654 Å^{-1} (Figure 2B and S8), which are assigned to the $(MA)_2Pb_3I_8 \cdot 2DMSO$ intermediate phase.[10,48,52] For the perovskite ink containing 0.05 wt% TAH, similar scattering peaks appear as early as ~16 s during the drying process (Figure S8 and S9), indicating a faster nucleation rate. Furthermore, when the TAH concentration is increased to 0.1 wt%, it takes an even shorter time of ~11 s to nucleate the intermediate complex. In the meantime, three new scattering peaks at q = 0.550, 0.564 and 0.674 Å^{-1} are observed (Figure 2B and S8). The strong scattering signal at q = 0.674 Å^{-1} is well agreed with the new peak located at 2θ = 9.48° measured from XRD (Figure S7), which is likely related to the new intermediate adduct of MAI-PbI_2-TAH. XRD and in-situ GIWAXS results indicate TAH tends to accelerate the nucleation process of the intermediate phases, which might arise from its

extra and stronger coordinate interaction with perovskite precursor compared with DMSO. Such the faster nucleation kinetics of intermediate complex is beneficial for the formation of dense perovskite grains (Figure S3).

The transparent intermediate complex of $(MA)_2Pb_3I_8 \cdot 2DMSO$ and MAI-PbI_2-TAH was converted into dark brown perovskite after thermal annealing (100°C). We in-situ studied the perovskite crystal growth kinetics during the annealing process with a time-resolved UV-vis absorption spectroscopy system. Figure 2C shows the color mapping of the UV-vis absorption spectra as a function of annealing time for the perovskite without and with 0.1 wt% TAH. We extracted the absorption intensity at the wavelength of 550 nm and plotted it as a function of annealing time (Figure 2D). In the pristine perovskite, the relatively unstable intermediate adduct with DMSO leads to unfavored quick crystal growth of perovskite within 75 s during the annealing process, which induces a discontinuous and inhomogeneous film morphology. On the contrary, the crystal growth is obviously retarded in TAH incorporated perovskite since extra energy is required to decompose the relative stable intermediate adduct with Pb^{2+}-SO_3^- coordination bonds, which is transformed into the black perovskite phase even beyond 240 s. Such the much slower crystal growth during thermal annealing in the TAH based perovskite allows the randomly formed nuclei to adjust their orientation to minimize the total Gibbs free energy and grow in a thermodynamically preferential orientation.[53]

The crystal structure of the annealed perovskite with different amount of TAH was also analyzed, as shown in Figure 3A. All of them display similar diffraction patterns, with a set of sharp peaks typical for the tetragonal $MAPbI_3$ phase. All of them show strong signals at 2θ = 14.08°, 28.40°, and 31.86°, assigned to the (110), (220), and (310) planes respectively. Several minor signals at 19.98°, 23.46°, 24.48°, 34.95°, 40.65°, 42.60°, and 43.17°, assigned to (112), (211), (202), (312), (224), (411), and

(314) planes respectively.[54] A small PbI_2 diffraction peak at 2θ = 12.67° is also observed in all three samples, because of 5 mol% excess PbI_2 in perovskite precursor recipe. It has been suggested that a moderate residual of excess PbI_2 can passivate the defects at perovskite surface and GBs and thus enhance the device performance. With the increased TAH concentration from 0 to 0.1 wt%, there is no shift for the diffraction peaks, revealing that TAH does not permeate into $MAPbI_3$ crystal lattice to induce a phase transition or form certain 2D structure at perovskite surface and GBs. Compared with the pristine perovskite, TAH based perovskites show stronger and sharper XRD peaks, with the full width at half maximum (FWHM) of (110) peak narrowed down from 0.252° to 0.201° (Figure S10). The XRD patterns also display an increased ratio of the intensity between (110) and (112) peaks when incorporated with TAH (7.04 for the pristine, 10.37 for the 0.05 wt% and 15.75 for the 0.1 wt%), which indicates a prominent (110) orientation (Figure 3A). The improved crystallinity and preferential (110) orientation in TAH based perovskite films are related to its stronger coordinate interaction and dominated precipitate of MAI-PbI_2-TAH adduct, which can further retard the perovskite crystallization and facilitate high-quality perovskites.

We further analyzed the surface and bulk crystallinity and the crystal orientation of annealed perovskite films with ex-situ GIWAXS measurements. Figure 3B shows the 2D GIWAXS patterns of the pristine and TAH incorporated perovskite films measured under incident angles (α_i) of 0.2° and 1° respectively. The scattering signal from the perovskite upper surface can be detected with a relatively small incident angle (e.g., α_i = 0.2°, penetration depth $Z_p \approx 100$ nm), while a large angle of 1° can probe the bulk information within the perovskite ($Z_p \approx 700$ nm, more details in Note S1, Supplemental Information). Thus, this technique is reliable to distinguish the surface signal from the bulk signal.[55] Figure 3C shows the polar intensity profiles along the (110) ring at $q \approx 1.00$ $Å^{-1}$ from the 2D GIWAXS

patterns of these two types of perovskite films measured at 0.2° and 1° respectively. The pristine perovskite exhibits almost an isotropic (110) ring in both surface and bulk patterns, while the bulk (α_i = 1°) (110) ring of the TAH based perovskite film concentrates along the out-of-plane (q_z) direction. It suggests a relatively dominant out-of-plane orientation with respect to the substrate for the perovskite grains, which is supposed to facilitate charge transport of PSCs in the vertical direction.[56] On the other hand, without new scattering ring detected, the surface signal in TAH based perovskite appears much decreased intensity than the bulk one (Figure S11), which is agreed well with the depth distribution of TAH from EDX and ToF-SIMS results.

Charged Defects Passivation

In order to investigate the charge recombination dynamics, steady-state photoluminescence (PL) and time-resolved photoluminescence (TRPL) decay measurements were performed on quartz substrate. Figure 4A shows the steady-state PL spectra of the respective perovskite films with different amount of TAH. Compared with the pristine perovskite, 0.05 wt% TAH incorporated perovskite exhibits stronger PL intensity by a factor of 320%, and the 0.1 wt% TAH based film further increases the PL intensity to a level of over 640%. In addition, TAH based perovskite films show blue-shifted PL peaks (770 nm for 0.05 wt% and 768 nm for 0.1 wt%) compared with the pristine perovskite (774 nm). We also measured the photoluminescence quantum yields (PLQYs) in the perovskite films with different amount of TAH. As shown in Figure S12A, compared with the pristine perovskite (3.08%), TAH incorporated perovskite film displays much higher PLQYs up to 5.94% for 0.05 wt% and 10.21% for 0.1 wt% TAH. Significantly enhanced PLQYs and blue-shifted PL peaks confirm the suppression of trap-assisted nonradiative recombination at perovskite surface and GBs induced by TAH.

TRPL decays of the corresponding perovskite films are shown in Figure 4B. Fitting the experimental data with the bi-exponential function:

$$I(t) = A_1 \exp\left(-\frac{t}{\tau_1}\right) + A_2 \exp\left(-\frac{t}{\tau_2}\right) \quad \text{(Equation 2)}$$

yields two decay times (*e.g.* τ_1 and τ_2), and the fitting parameters are summarized in Table S1. The fast decay lifetime (τ_1) is likely related to the charge trapping process at perovskite surface, while the slow decay lifetime (τ_2) represents the de-trapping or recombination process in the bulk.[57,58] It should be noted that the excitation fluence in our study is very low ($\leq$ 5 nJ/cm^2), which only generates much lower density of free carriers (2.4 × 10^{14} cm^{-3}) compared with that of trap states. In this condition, TRPL decay mainly responds the trapping and nonradiative recombination behaviors (Figure 4C, Figure S12, Table S2 and S3, more details in Note S2, Supplemental Information).[59] Compared with the pristine perovskite film with relatively short lifetime (99.26 ns), TAH based perovskites exhibit prolonged average lifetime (217.07 ns for 0.05 wt% and 344.78 ns for 0.1 wt% TAH), which indicates better quality of perovskite crystal with lower density of trap states. Moreover, the proportion of the fast decay is significantly reduced when TAH is incorporated into the perovskite (55.9% for the pristine, 17.8% for 0.05 wt% and 7.1% for 0.1 wt% TAH), which further confirms the strongly suppressed nonradiative recombination at perovskite surface (Table S1).

Several measurements were carried out to verify the interaction between the zwitterionic moieties in TAH and charged defects in the perovskite. We first conducted X-ray photoelectron spectroscopy (XPS) to investigate the coordinate interaction. Figure S13 shows the typical XPS survey for the pristine and TAH incorporated perovskites. In order to confirm whether there was remnant of TAH in the annealed perovskite film, we examined the O 1s XPS spectra in these two samples. While negligible O 1s signal in the pristine perovskite, an obvious O 1s peak at 532.3 eV is detected in the

TAH incorporated perovskite, which confirms the existence of TAH after thermal annealing. In addition, both of the Pb $4f_{7/2}$ and Pb $4f_{5/2}$ peaks (at 138.7 and 143.6 eV respectively) detected in the pristine perovskite are shifted to the direction with lower binding energy by ~0.3 eV in the 0.1 wt% TAH based perovskite (Figure 4D). Such a negative shift of Pb 4f signal indicates the decreased cationic charge of under-coordinated Pb^{2+} within the perovskite, which is likely due to the donation of lone pair electrons within the sulfonate groups (SO_3^-) in TAH through the coordinate interaction.[60,61]

Fourier transform infrared spectroscopy (FTIR) was also performed to confirm this interaction between sulfonate zwitterion and under-coordinated Pb^{2+} in the annealed perovskite films, as shown in Figure 4E. The FTIR spectrum for the pure TAH film shows two peaks located at ~1035 and 1184 cm^{-1}, which represent the symmetric and asymmetric stretching vibrations of S=O (υ_s and υ_{as}) in SO_3^-.[62] These two peaks shift to higher wavenumber of ~1045 and 1190 cm^{-1} respectively when TAH is incorporated in to the perovskite. In comparison, these vibration signals of S=O cannot be detected in the pristine perovskite, indicating the volatile of DMSO during the annealing process. The increased wavenumber of S=O stretching vibration stems from the decreased spatial symmetry of SO_3^- in TAH after coordinate interaction with under-coordinated Pb^{2+}, thus the symmetric and asymmetric stretching vibrations become harder.[63] This result indicates the coordination between sulfonate groups in TAH and under-coordinated Pb^{2+} in the perovskite even after the thermal annealing, confirming its strong capability to passivate charged defects at perovskite surface and GBs.

Space charge limited current (SCLC) analysis based on electron-only devices with the structure of ITO/SnO_2/PVSK/$PC_{61}BM$/Au was carried out to estimate the electron trap density (N_t) and electron mobility (μ_e) respectively in different regimes, as shown in Figure 4F. The trap-filled limit voltage (V_{TFL}) determined as the onset voltage of TFL regime (n > 3) can be used to calculate N_t with the

equation:[64]

$$N_t = 2\varepsilon_0\varepsilon_r V_{TFL}/qL^2 \quad \text{(Equation 3)}$$

in which ε_0 is the vacuum permittivity, ε_r is the relative permittivity of perovskite, which can be taken as the value of 18 for $MAPbI_3$ from a previous work,[65] and L is the thickness of the perovskite film. Compared with the pristine perovskite (N_t = 1.28 × 10^{16} cm^{-3}), TAH incorporated perovskite film relatively lower trap density (N_t = 0.94 × 10^{16} cm^{-3}), which confirms TAH's efficient passivation of charged defects at perovskite surface and GBs. Charge transport property in the perovskite films incorporated with TAH can be also estimated in the trap-free regime (n = 2) with the equation:[66]

$$J = (9\mu_e\varepsilon_0\varepsilon_r V^2)/8L^3 \quad \text{(Equation 4)}$$

Compared with the pristine perovskite (μ_e = 2.2 × 10^{-2} cm^2 V^{-1} s^{-1}), TAH incorporated perovskite exhibits higher electron mobility of 3.9 × 10^{-2} cm^2 V^{-1} s^{-1} in the vertical direction, mainly due to the significant improved film quality with higher crystallinity and relatively preferential out-of-plane orientation.[56]

Photovoltaic Device Performance

We fabricated inverted p-i-n PSCs through meniscus-guided blade coating technique using the perovskite ink incorporated with zwitterionic surfactant TAH. The inverted PSCs are assembled with the structure of ITO/PTAA/TAH-$MAPbI_3$/$PC_{61}BM$/bathophenanthroline (BCP)/Ag, where a ~400 nm thick uniform and pinhole-free perovskite film is sandwiched between PTAA HTL and $PC_{61}BM$ electron transport layer (ETL) (Figure 5A). Figure 5B shows the schematic energy levels diagrams of corresponding components in the p-i-n PSCs, which are calculated from ultraviolet photoelectron spectra (UPS), as shown in Figure S14. Band structure parameters are also summarized in Table S4.

Compared with the pristine perovskite, the work function, HOMO and LUMO energy levels of TAH based perovskite are shifted up to 0.09, 0.12 and 0.12 eV respectively, which might be attributed to the formation of interfacial dipole induced by TAH at the upper surface of perovskite (Figure S15).

The photovoltaic parameters of $MAPbI_3$ based perovskite incorporated with different amounts of TAH are summarized in Table 1. With the increase of TAH concentration from 0 to 0.2 wt%, the V_{OC} is significantly and monotonically enhanced from 1.067 V to 1.131 V, which clearly shows the TAH's excellent capability to passivate charged defects at perovskite surface and GBs. The short-circuit current density (J_{SC}) and fill factor (FF) begin to drop when more (0.2 wt%) TAH is incorporated, which indicates the devices with excess TAH start to suffer from inferior charge extraction and transport due to the excess alkyl chain assembled at the surface and GBs of perovskite films (Figure S16A). This is not a drawback, as 0.1 wt% TAH already enables high-quality coating of perovskite films. Figure 5C shows the *J-V* curves of the champion devices with and without TAH. An anti-reflection (AR) MgF_2 film is deposited on the incident side of ITO/glass substrate to improve the transmittance of substrates (Figure S16B). The control devices based on pristine $MAPbI_3$ show a maximum PCE of 19.34%, with a V_{OC} of 1.067 V, a J_{SC} of 23.27 mA/cm^2, and an FF of 77.90%. In comparison, the devices incorporated with 0.1 wt% TAH in the ink exhibit the highest efficiency, with a maximum PCE up to 22.07%, an obviously enhanced V_{OC} of 1.126 V, a J_{SC} of 24.13 mA/cm^2, and an FF of 81.22%. The improved photovoltaic performance is mainly attributed to the high-quality perovskite films with high crystallinity and preferred orientation, as well as the efficient passivation of charged defects at both perovskite surface and GBs assisted with zwitterionic surfactant TAH. The integrated J_{SC} from external quantum efficiency (EQE) measurement for the control and TAH based devices are 22.06 and 23.13 mA/cm^2 respectively (Figure 5D), which are consistent with those

measured from *J*-*V* curves.

Figure S17A and B shows the hysteresis behavior in *J*–*V* curves for the PSCs with and without TAH under forward and reverse scanning, respectively. Generally, hysteresis is ascribed to the interfacial capacitance, which is originated from unbalanced charge extraction, high density of trap states at perovskite surface, and ion migration. TAH based device shows negligible hysteresis in *J*–*V* curves with a hysteresis index (($PCE_{Reverse}-PCE_{Forward}$)/$PCE_{Reverse}$) of barely 0.4%, which is lower than that of the control device (2.1%). The elimination of hysteresis effect is mainly attributed to the efficient passivation of charged defects at perovskite surface and GBs. Figure S17C shows the steady-state photocurrent outputs and stabilized PCEs for the devices with and without TAH, which are measured under their maximum power points (MPPs). The TAH based device exhibits a stabilized photocurrent of 22.86 mA/cm^2 at 0.96 V bias, with a stabilized efficiency of 21.95%, which is consistent with the efficiency from the *J*–*V* curves. The control device exhibits a relatively lower stabilized photocurrent of 21.31 mA/cm^2 at 0.90 V bias, with a stabilized efficiency of 19.18%.

To understand the mechanism behind the significantly improved V_{OC} in the TAH based devices, we measured the external quantum efficiency of electroluminescence (EQE_{EL}) for a complete PSC operating as a light-emitting diodes (LED) in forward voltage bias, which has been extensively utilized to estimate the V_{OC} deficit.[5,67] For the purpose of evaluating V_{OC}, the EQE_{EL} is measured when the injection current (dark recombination current) equals the J_{SC} under simulated 1-sun illumination. A large EQE_{EL} indicates a large ratio of injection current resulting in photo emission, suggesting low non-radiative recombination. The theoretical radiative limit of V_{OC} ($V_{OC,rad}$) can be calculated from the reciprocity relation between the photovoltaic external quantum efficiency (EQE_{PV}) and EQE_{EL} according to the equations:[68,69]

$$V_{\mathrm{OC,rad}} = \frac{k_{\mathrm{B}}T}{q}\ln\left(\frac{\int \mathrm{EQE_{PV}}(E)\times\phi_{\mathrm{AM1.5}}(E)\mathrm{d}E}{\int \mathrm{EQE_{PV}}(E)\times\phi_{\mathrm{BB}}(E)\mathrm{d}E}+1\right) = \frac{k_{\mathrm{B}}T}{q}\ln\left(\frac{J_{\mathrm{SC}}}{J_0^{rad}}+1\right) \qquad \text{(Equation 5)}$$

in which $\phi_{\mathrm{AM1.5}}$ and ϕ_{BB} refer to the solar AM 1.5 spectrum and black-body radiation spectrum at 300 K respectively, and J_0^{rad} refers to the radiative emission photocurrent density in the dark. Following detailed balance model, $V_{\mathrm{OC,rad}}$ has been calculated to be 1.30 V for $MAPbI_3$ with a bandgap of 1.59 eV.[70] In a real PSC, additional non-radiative recombination loss should be considered according to the equation:[5,71]

$$V_{\mathrm{OC}} = V_{\mathrm{OC,rad}} - \Delta V_{\mathrm{OC,nr}} = V_{\mathrm{OC,rad}} + \frac{k_{\mathrm{B}}T}{q}\ln \mathrm{EQE_{EL}} \qquad \text{(Equation 6)}$$

in which $\Delta V_{\mathrm{OC,nr}}$ refers to the non-radiative recombination loss, and $\mathrm{EQE_{EL}}$ refers to the external quantum efficiency of electroluminescence under an injection current density equal to J_{SC}. As shown in Figure 5E and 5F, we tested the control and TAH based PSCs operating as LEDs under voltage bias from 0 to 2 V. TAH based device starts to work under 1.1 V voltage bias, and it shows an $\mathrm{EQE_{EL}}$ of 0.14% at a driving current equal to the J_{SC} (Figure S18A), corresponding to a $\Delta V_{\mathrm{OC,nr}}$ of 170 mV. The calculated V_{OC} in the TAH based device (1.13 V) agrees well with the V_{OC} measured in *J-V* curve (~1.13 V). In comparison, the control device shows a much lower $\mathrm{EQE_{EL}}$ of 0.0044% at a driving current equal to the J_{SC}, corresponding to a much higher $\Delta V_{\mathrm{OC,nr}}$ of 260 mV. This result indicates that non-radiative recombination in the TAH incorporated perovskite has been significantly suppressed mainly because of its strong coordinate interaction with the charged defects.

Mott–Schottky (M-S) analysis was carried out to estimate the V_{bi} of the control and TAH based devices, as shown in Figure 5G. The relationship between the junction capacitance and DC voltage bias can be described by the equation:[72]

$$\frac{A^2}{C^2} = \frac{2(V_{bi}-V)}{q\varepsilon_0\varepsilon N} \qquad \text{(Equation 7)}$$

in which A is the active area of the device, q is the elementary charge, ε_0 and ε refer to vacuum and

relative permittivity respectively, N refers to the impurity doping density, and V refers to the applied DC voltage. V_{bi} can be calculated using the intercept of linear regime of M-S plot with the x axis. The fitting result shows a larger V_{bi} for the TAH based device (0.97 V) compared with the control device (0.92 V), which follows a trend similar to the V_{OC} measured in *J-V* curves. In TAH incorporated perovskite, TAH prefers to anchor at the upper surface of perovskite, which induces the formation of interfacial dipole with its negative moieties (SO_3^-) towards perovskite and positive moieties (NH_4^+) towards outside. This dipole is aligned with the direction of built-in field in PSCs. The superposition of built-in field and the interfacial dipole leads to a greater local electric field, which enhances the V_{bi} (Figure S15).[73]

We further quantitatively estimated the energetic distribution of trap density (N_t) using temperature dependent admittance spectroscopy (TAS) combined with Mott-Schottky analysis.[74,75] Figure S18B displays the capacitance spectra as a function of AC frequency for the control and TAH based devices, applied by an AC voltage of 50 mV with the frequency decrease from 10^6 to 100 Hz (more details in Note S3, Supplemental Information). As shown in Figure 5H, for the control device, the energetic trap density distribution peak is 5.74×10^{16} cm^{-3} eV^{-1} centered at the energy depth of 0.42 eV, while that of the TAH based device is reduced to 4.21×10^{16} cm^{-3} eV^{-1} located at 0.40 eV. The energetic distribution of trap states can be fitted by Gaussian distribution, and the integrated N_t for the control devices is calculated to be 6.83×10^{15} cm^{-3}, which is 1.27 times larger than that of the TAH based device (5.36×10^{15} cm^{-3}). TAS result suggests that deep trap states at the surface of pristine perovskite are efficiently suppressed with the incorporation of TAH in the perovskite ink.

In order to examine the universality of additive engineering using TAH zwitterionic surfactant in the meniscus coating of different types of PSCs, we investigated the mixed triple-cation perovskite

(CsFAMA) system in the conventional n-i-p architecture. Figure S19A and Table S5 show the *J-V* curves and photovoltaic parameters of the best-performing control and TAH based devices with conventional n-i-p planar structure of FTO/SnO_2/TAH-PVSK/Spiro-OMeTAD/Au. Compared with the control devices, 0.1 wt% TAH based devices exhibit superior photovoltaic performance with simultaneous increase in V_{OC}, J_{SC} and FF, yielding a maximum PCE up to 22.20%. This significant improvement is coincident well with the trend in inverted p-i-n devices. It should be noted that a very high V_{OC} up to 1.205 V is obtained for the TAH based devices, corresponding to a small V_{OC} deficit of 0.405 V for ~1.61 eV bandgap of CsFAMA based perovskite.[76] Large-area PSCs are crucial for the development of low-cost perovskite modules. We also blade coated perovskite films in relatively large area with a dimension of 3 cm × 2 cm (Figure S19B) and built the conventional n-i-p architecture with enlarged active area from 0.04 to 0.8 cm^2. Figure 5I displays the *J-V* curves of the champion TAH incorporated PSCs with 0.8 cm^2 active area, which shows a superior PCE of 21.02% and a stabilized PCE of 20.93% under MPP of 0.98 V (Table S5 and Figure S19B).

We summarized the state-of-the-art PCEs as a function of processing temperature for the deposition of perovskite photovoltaic films through different scalable printing techniques published in the previous works, as shown in Figure S20 and Table S6. It is worth noting that this work (red star, RT coating) reaches one of the highest records for the upscaling coated PSCs (substrate temperature from RT to 150°C), not limited in RT coated ones. Compared with our previous work (red dot), here we focus on the perovskite ink multifunctional formulation and achieve significant increase of PCEs from 20% to over 22%.[26] As far as we known, this work is also among the top performances for the $MAPbI_3$ based PSCs, regardless of the deposition methods. This result suggests an efficient and universal additive strategy using TAH zwitterionic surfactant in the RT meniscus coating of perovskite films for

both the inverted and conventional structured devices in relatively large area.

Water-Resistant Perovskite Films and Device Stability

Organic-inorganic halide perovskites are highly sensitive to moisture and can be decomposed readily in high humidity environment. In order to examine the water-resistant performance of perovskite with TAH strategy, we first measured the static water contact angles on the surface of pristine and 0.1 wt% TAH incorporated perovskite (Figure S21A). TAH incorporated perovskite surface exhibits relatively larger water contact angle (42.6°) compared with that on the pristine perovskite (33.9°). The dynamic dissolving process of water droplet on the surface of these two perovskites was also recorded, as shown in Figure 6A. The pristine perovskite is immediately decomposed to PbI_2 when contacted with water droplet, while the TAH incorporated perovskite film becomes much more water-resistant. Considering the amphipathic nature of TAH molecule, TAH molecules prefer to self-assemble at surface of perovskite with the hydrophobic alkyl chains intertwining, spontaneously inducing the formation of a moisture barrier and facilitates inner encapsulation.[77]

The moisture stability of the pristine and TAH incorporated perovskite films was studied by exposing them under relatively high RH of 60±10% at 25±5°C for 14 days. The evolution of perovskite phase was tracked by XRD, as shown in Figure S21B. For the pristine perovskite, the XRD pattern appears two obvious peaks at 8.5° and 10.5° after 14 days aging, which can be assigned to a perovskite hydrate $(CH_3NH_3)_4PbI_6{\cdot}2H_2O$. This hydrate is a pale yellow crystalline solid, and it has been suggested that the transition from $MAPbI_3$ to $(CH_3NH_3)_4PbI_6{\cdot}2H_2O$ hydrate occurs readily upon exposure to humid air.[78] The intensity of PbI_2 diffraction peak at 12.6° is also increased in the pristine

perovskite, suggesting obvious decomposition into PbI_2. In comparison, the diffraction pattern of TAH incorporated perovskite is almost identical after exposure to high RH over 14 days, and only trace amount of perovskite hydrate can be detected. Superior moisture stability of TAH based perovskite is mainly attributed to the self-assembly and intertwining of hydrophobic alkyl chains at perovskite upper surface.

$MAPbI_3$ is the original but less stable perovskite composition in most of high efficiency PSCs. Inverted p-i-n structured $MAPbI_3$ based PSCs were used to evaluation the device stability with this multifunctional additive strategy. The ambient storage, thermal stressing, as well as light illumination stability of the blade-coated devices were investigated in detail under different aging conditions, as shown in Figure 6. Ambient stability of the unencapsulated devices was tracked under 25±5°C and 20±5% RH. TAH based devices show much better shelf stability, which still retain an average PCE over 21% (96.7% of initial PCE) after 1200 h. In comparison, the control devices only maintain an average PCE of 10.5% (54.7% of initial PCE) under the same condition. Thermal stability was recorded during the aging process of the control and TAH based devices at 80°C in the glovebox. TAH based devices display superior thermal stability, maintaining 92.0% of their initial efficiencies on average after 672 h ageing, compared to only 55.2% for the control devices. Light illumination stability of the encapsulated devices was also examined under continuous illumination at 40±5°C and 50±5% RH. After 600 h light soaking under 0.7 sun, TAH based devices keep 90.3% of their initial efficiencies on average, which are much higher than those of the control devices (53.5%). Since the charged defects at perovskite surface and GBs are one of the main reasons for the accelerated deterioration in moisture, the enhanced stability of TAH based devices under different aging conditions is mainly attributed to the efficient defects passivation as well as the robust moisture barrier at perovskite surface with the

assist of TAH strategy.

Conclusions

In summary, we have demonstrated a facile and multifunctional zwitterionic surfactant strategy incorporated into the perovskite ink which successfully enabled the room-temperature meniscus coating of high-quality perovskite photovoltaic films. TAH facilitated dense perovskite films with fully coverage, modulated perovskite crystallization kinetics and orientation, neutralized charged defects, and spontaneously self-assembled a robust moisture barrier at perovskite upper surface. Universality and versatility of this strategy not only enabled the enhanced efficiencies up to 22% (0.04 cm^2 active area) and 21% (0.8 cm^2) across perovskite compositions and device architectures, but also significantly enhanced the moisture, thermal and light illumination stability simultaneously. Further understanding the synergistic role of functionalized surfactants in the large-scale printing of perovskite polycrystalline films will offer us a new pathway towards scalable manufacture of perovskite based optoelectronic devices with superior performance and stability.

EXPERIMENTAL PROCEDURES

Resource Availability

Lead Contact

Further information and requests for resources and materials should be directed to and will be fulfilled by the Lead Contact, Gang Li (gang.w.li@polyu.edu.hk).

Materials Availability

This study did not generate new unique materials.

Data and Code Availability

The data presented in this work are available from the corresponding authors upon reasonable request.

Materials

Unless stated otherwise, chemicals and solvents were obtained commercially and were used without further purification, including tetradecyldimethyl(3-sulfopropyl)ammonium hydroxide inner salt (TAH) (Tokyo Chemical Industry, 98.0%), lead iodide (PbI_2) (TCI, 99.99%), methylammonium iodide (MAI) and methylammonium chloride (MACl) (Xi'an Polymer Light Technology Corp., 99.5%), poly[bis(4-phenyl)(2,4,6-trimethylphenyl)amine (PTAA) ($M_n \leq 6000$, Xi'an Polymer Light Technology Corp.), $PC_{61}BM$ (99.5%, Solenne BV) and bathophenanthroline (BCP) (98%, Alfa Aesar). All solvents including *N*,*N*-dimethylformamide (DMF) (99.8%, anhydrous), dimethyl sulfoxide (DMSO) (99.9%, anhydrous), chlorobenzene (99.8%, anhydrous), toluene (99.8%, anhydrous) and 2-propanol (99.5%, anhydrous) were purchased from Sigma-Aldrich.

Device Fabrication

Laser-patterned ITO/glass substrates (sheet resistance ≈ 12 Ω per square) were pre-cleaned using an ultrasonicator and subjected with ultraviolet–ozone treatment for 20 min. For the inverted p-i-n structured PSCs, PTAA hole transport layer (HTL) was spin-coated on the pre-cleaned ITO substrate using the PTAA solution (5 mg/mL in toluene) at 5000 rpm and annealed at 100°C for 10 min. $MAPbI_3$ based perovskite precursor solution was prepared with 1.15 M PbI_2, 1.1 M MAI and 0.05 M MACl dissolved in the mixture solvent of DMF and DMSO (9:1, v:v). We prepared the TAH's mother solution in the mixture solvent of DMF and DMSO (9:1, v:v, 20 mg/mL) and stirred it overnight. According to

different concentration of TAH in perovskite precursor solution (0, 0.02, 0.05, 0.1, and 0.2 wt%), we added 0, 16, 40, 80, and 160 μL of TAH mother solution into 1 mL perovskite precursor solution respectively and stirred the mixture solution for 1 h. Small droplet of perovskite ink (5 μL) was dripped on the substrate and swiped linearly by a film applicator at the speed of 10 mm/s. The gap between the film applicator and substrate was set as 100 μm. A laminar nitrogen knife was installed right next to the blade substrate with the flow parallel to the substrate. The as-prepared wet perovskite film was gas-quenched by the nitrogen knife with the fixed nitrogen blow rate of 40 m/s (calibrated using the Testo 416 flowmeter), in order to remove the extra precursor solution and induce the precipitate of perovskite intermediate adducts. The intermediate films were transferred onto a hotplate and annealed at 100°C for 30 min. $PC_{61}BM$ electron transport layer (ETL) was spin-coated on the top of perovskite film using $PC_{61}BM$ solution (20 mg/mL in chlorobenzene). The inverted devices were finished by thermal evaporating 80 nm thick Ag counter electrode under a pressure of 10^{-6} Torr. For the conventional n-i-p structured PSCs, a thin layer of SnO_2 nanoparticles was spin-coated onto the pre-cleaned ITO substrate using a SnO_2 colloidal dispersion solution in water (5 wt%) at 5000 rpm and annealed at 150°C for 30 min in ambient atmosphere. Mixed triple-cation (CsFAMA) perovskite precursor solution was prepared with 1.2 M PbI_2, 1.1 M FAI, 0.2 M $PbBr_2$, 0.2 M MABr and 0.05 M CsI dissolved in the mixture solvent of DMF and DMSO (8:2, v:v). Spiro-OMeTAD HTL was spin-coated on the top of perovskite using its solution (80 mg/mL in chlorobenzene) with 29 μL of tBP and 17.5 μL of Li-TFSI (520 mg/mL in acetonitrile). Finally, an 80 nm thick Au electrode was deposited by thermal evaporation using a shadow mask to pattern the electrodes. We encapsulated the devices in the nitrogen glovebox. Epoxy resin AB glue (Super Glue Corp.) was used for device edge sealing with a cover glass. The devices were further dried at RT for 10 min to allow complete solidification of the

AB glue.

Characterizations

Film morphology of the perovskite was examined using a high-resolution field emission SEM (JEOL JSM-6335F). AFM height images were obtained using a Bruker Multimode 8 scanning probe microscope (tapping mode). ToF-SIMS depth analysis was conducted using Model TOF-SIMS V, ION-TOF GmbH with pulsed primary ions from a Cs^+ (3 keV) liquid-metal ion gun and a Bi^+ pulsed primary ion beam for the analysis (25 keV). Crystalline structure was investigated on a Rigaku SmartLab X-ray diffractometer with Cu Kα radiation in a step of 0.01° and θ-2θ scan mode from 5° to 50°. GIWAXS was carried out using a Xeuss 2.0 SAXS/WAXS laboratory beamline with a Cu X-ray source (8.05 keV, 1.54 Å) and a Pilatus3R 300K detector. In-situ GIWAXS was conducted by a 23A small- and wide-angle X-ray scattering beamline at the National Synchrotron Radiation Research Center (NSRRC), Hsinchu, Taiwan. The wavelength of X-ray was kept at 1.239 Å (10 keV) and the time-resolved scattering signals were collected by a C9728DK area detector. The incident angle was kept at 2° to enhance the signal resolution with a frame exposure time of 1 s. The in-situ UV-vis absorption spectra were obtained using a F20-UVX spectrometer (Filmetrics, Inc.) equipped with tungsten halogen and deuterium light sources (Filmetrics, Inc.). UV-vis absorption spectra were measured by a UV-vis spectrophotometer (CARY5000, Varian). Steady-state PL spectra and TRPL transient decay were measured using a PL spectrometer (Edinburgh Instruments, FLS 900) with the excitation of a 636.2 nm picosecond pulsed diode laser (EPL-635, ~5 nJ/cm^2). PLQYs were measured using a commercialized PLQY system (LQ-100, Enli Technology Co. Ltd., Taiwan), which consists of a 405 nm LED excitation source (0.65 mW/cm^2), a PTFE integrating sphere, a H-sCMOS 2048

multichannel spectrometer and optical fibers. The integration time was set as 300 ms. FTIR spectra were measured with an attenuated total refraction (ATR) spectrometer (PerkinElmer Spectrum 100, USA) from 4000 to 400 cm^{-1} with a resolution of 4 cm^{-1}. UPS and XPS measurement were carried out by a VG ESCLAB 220i-XL surface analysis system equipped with a monochromatic Al Kα X-ray source (1486.6 eV) in a vacuum of 3.0×10^{-8} Torr. For the completed devices, *J-V* curves were obtained using a Keithley 2400 Source Meter under standard AM 1.5 G illumination (Enli Technology Co. Ltd., Taiwan), and the light intensity was calibrated by a standard KG-5 Si diode. Both forward (from −0.2 to 1.2 V) and reverse scanning (from 1.2 to −0.2 V) were performed with a delay time of 100 ms. Small-area devices have the active area of 0.04 cm^2 confined by the crossed area of counter electrode and ITO stripe. Relatively large-area devices have the active area of 0.8 cm^2. An anti-reflection (AR) MgF_2 film is deposited on the incident side of ITO/glass substrate. EQE spectra were measured with a QE-R 3011 EQE system (Enli Technology Co. Ltd., Taiwan) using 100 Hz chopped monochromatic light ranging from 300 to 850 nm. The EL EQE spectra were recorded by a LED photo-luminescence quantum yield measurement system (Enli Tech LQ-100) equipped with Keithley 2400 Source Measure Unit. Mott–Schottky analysis was examined using a CHI660e electrochemical workstation at 100 kHz with the DC bias potential ranging from 0 to 1.3 V under dark conditions. Admittance spectra were obtained using an impedance analyzer (Hioki E. E. Corp., Model 3532-50 LCR HiTESTER). An AC modulation of an amplitude of 50 mV was superimposed at the frequency decreased from 10^3 to 0.1 kHz in dark.

SUPPLEMENTAL INFORMATION

Supplemental Information can be found online at https://doi.org//j.joule.2020.xx.xxx.

ACKNOWLEDGMENTS

This work was supported by Research Grants Council of Hong Kong (Grant Nos. 15246816 and C5037-18G), RGC Postdoctoral Fellowship Scheme (3-RA54, K. Liu); Shenzhen Science and Technology Innovation Commission (Project No. JCYJ20170413154602102), the Project of Strategic Importance (Project No. 1-ZE29), University Supporting Fund for Major Research (1-BBAS) and Sir Sze-yuen Chung Endowed Professorship Fund (8-8480) provided by the Hong Kong Polytechnic University; X. Lu and M. Qin acknowledge the financial support from Research Grant Council of Hong Kong (RGC) (General Research Fund No. 14314216). All authors are grateful for the beam time and technical support provided by 23A SWAXS beamline at NSRRC, Hsinchu.

AUTHOR CONTRIBUTIONS

K. L. and G. L. conceived the paper. K. L. and Q. L. carried out solar cell fabrication and part of characterization. M. Q. and X. L. performed in-situ and ex-situ GIWAXS and analyzed the data. H. Y. and S. K. S. examined the TAS analysis. D. S. and C. S. L. conducted XPS measurement. Y. Z. and Z. Z. measured static water contact angles and Mott-Schottky analysis. H. Z., Z. R. and J. H. assisted with XRD, SEM, PL, and FTIR measurements. P. W. K. F. assisted with in-situ UV-vis absorption analysis. Z. W. and J. H. assisted with fluence- and wavelength-dependent TRPL decays. K. L., X. L. and G. L. wrote the manuscript. All authors made a substantial contribution to the discussion of the content and reviewed and edited this manuscript before submission. G. L. and X. L. supervised this work.

DECLARATION OF INTERESTS

The authors declare no competing interests.

REFERENCES

1. Gratzel, M. (2014). The light and shade of perovskite solar cells. Nat. Mater. *13*, 838-842.
2. Green, M.A., Ho-Baillie, A., and Snaith, H.J. (2014). The emergence of perovskite solar cells. Nat. Photonics *8*, 506-514.
3. Correa-Baena, J.-P., Abate, A., Saliba, M., Tress, W., Jesper Jacobsson, T., Grätzel, M., and Hagfeldt, A. (2017). The rapid evolution of highly efficient perovskite solar cells. Energy Environ. Sci. *10*, 710-727.
4. National Renewable Energy Laboratory (NREL) (2019). Best research-cell efficiency chart. https://www.nrel.gov/pv/assets/pdfs/best-research-cell-efficiencies.20191106.pdf.
5. Saliba, M., Matsui, T., Domanski, K., Seo, J.-Y., Ummadisingu, A., Zakeeruddin, S.M., Correa-Baena, J.-P., Tress, W.R., Abate, A., Hagfeldt, A., et al. (2016). Incorporation of rubidium cations into perovskite solar cells improves photovoltaic performance. Science *354*, 206-209.
6. Wu, Y., Xie, F., Chen, H., Yang, X., Su, H., Cai, M., Zhou, Z., Noda, T., and Han, L. (2017). Thermally stable MAPbI3 perovskite solar cells with efficiency of 19.19% and area over 1 cm(2) achieved by additive engineering. Adv. Mater. *29*, 1701073.
7. Tan, H., Jain, A., Voznyy, O., Lan, X., de Arquer, F.P.G., Fan, J.Z., Quintero-Bermudez, R., Yuan, M., Zhang, B., Zhao, Y., et al. (2017). Efficient and stable solution-processed planar perovskite solar cells via contact passivation. Science *355*, 722-726.
8. Yang, M., Li, Z., Reese, M.O., Reid, O.G., Kim, D.H., Siol, S., Klein, T.R., Yan, Y., Berry, J.J., van Hest, M.F.A.M., et al. (2017). Perovskite ink with wide processing window for scalable high-efficiency solar cells. Nat. Energy *2*, 17038.
9. Yang, G., Chen, C., Yao, F., Chen, Z., Zhang, Q., Zheng, X., Ma, J., Lei, H., Qin, P., Xiong, L., et al. (2018). Effective carrier-concentration tuning of SnO2 quantum dot electron-selective layers for high-performance planar perovskite solar cells. Adv. Mater. *30*, 1706023.
10. Jeon, N.J., Noh, J.H., Kim, Y.C., Yang, W.S., Ryu, S., and Seok, S.I. (2014). Solvent engineering for high-performance inorganic-organic hybrid perovskite solar cells. Nat. Mater. *13*, 897-903.
11. Xiao, M., Huang, F., Huang, W., Dkhissi, Y., Zhu, Y., Etheridge, J., Gray-Weale, A., Bach, U.,

Cheng, Y.B., and Spiccia, L. (2014). A fast deposition-crystallization procedure for highly efficient lead iodide perovskite thin-film solar cells. Angew. Chem. Int. Ed. Engl. *53*, 9898-9903.

12. Kim, M., Kim, G.-H., Lee, T.K., Choi, I.W., Choi, H.W., Jo, Y., Yoon, Y.J., Kim, J.W., Lee, J., Huh, D., et al. (2019). Methylammonium chloride induces intermediate phase stabilization for efficient perovskite solar cells. Joule *3*, 2179-2192.
13. Yang, M., Zhou, Y., Zeng, Y., Jiang, C.S., Padture, N.P., and Zhu, K. (2015). Square-centimeter solution-processed planar CH3NH3PbI3 perovskite solar cells with efficiency exceeding 15%. Adv. Mater. *27*, 6363-6370.
14. Ye, F., Chen, H., Xie, F., Tang, W., Yin, M., He, J., Bi, E., Wang, Y., Yang, X., and Han, L. (2016). Soft-cover deposition of scaling-up uniform perovskite thin films for high cost-performance solar cells. Energy Environ. Sci. *9*, 2295-2301.
15. Chen, H., Ye, F., Tang, W., He, J., Yin, M., Wang, Y., Xie, F., Bi, E., Yang, X., Gratzel, M., et al. (2017). A solvent- and vacuum-free route to large-area perovskite films for efficient solar modules. Nature *550*, 92-95.
16. Barrows, A.T., Pearson, A.J., Kwak, C.K., Dunbar, A.D.F., Buckley, A.R., and Lidzey, D.G. (2014). Efficient planar heterojunction mixed-halide perovskite solar cells deposited via spray-deposition. Energy Environ. Sci. *7*, 2944-2950.
17. Mohamad, D.K., Griffin, J., Bracher, C., Barrows, A.T., and Lidzey, D.G. (2016). Spray-cast multilayer organometal perovskite solar cells fabricated in air. Adv. Energy Mater. *6*, 1600994.
18. Schmidt, T.M., Larsen-Olsen, T.T., Carlé, J.E., Angmo, D., and Krebs, F.C. (2015). Upscaling of perovskite solar cells: fully ambient roll processing of flexible perovskite solar cells with printed back electrodes. Adv. Energy Mater. *5*, 1500569.
19. Hwang, K., Jung, Y.S., Heo, Y.J., Scholes, F.H., Watkins, S.E., Subbiah, J., Jones, D.J., Kim, D.Y., and Vak, D. (2015). Toward large scale roll-to-roll production of fully printed perovskite solar cells. Adv. Mater. *27*, 1241-1247.
20. Deng, Y., Peng, E., Shao, Y., Xiao, Z., Dong, Q., and Huang, J. (2015). Scalable fabrication of efficient organolead trihalide perovskite solar cells with doctor-bladed active layers. Energy Environ. Sci. *8*, 1544-1550.
21. Yang, Z., Chueh, C.-C., Zuo, F., Kim, J.H., Liang, P.-W., and Jen, A.K.Y. (2015). High-performance fully printable perovskite solar cells via blade-coating technique under the ambient

condition. Adv. Energy Mater. *5*, 1500328.

22. Liao, H.-C., Guo, P., Hsu, C.-P., Lin, M., Wang, B., Zeng, L., Huang, W., Soe, C.M.M., Su, W.-F., Bedzyk, M.J., et al. (2017). Enhanced efficiency of hot-cast large-area planar perovskite solar cells/modules having controlled chloride incorporation. Adv. Energy Mater. *7*, 1601660.
23. Zhong, Y., Munir, R., Li, J., Tang, M.-C., Niazi, M.R., Smilgies, D.-M., Zhao, K., and Amassian, A. (2018). Blade-coated hybrid perovskite solar cells with efficiency > 17%: an in situ investigation. ACS Energy Lett. *3*, 1078-1085.
24. Li, X., Bi, D., Yi, C., Décoppet, J.-D., Luo, J., Zakeeruddin, S.M., Hagfeldt, A., and Grätzel, M. (2016). A vacuum flash–assisted solution process for high-efficiency large area perovskite solar cells. Science *353*, 58-62.
25. Kim, G.M., and Tatsuma, T. (2016). Semitransparent solar cells with ultrasmooth and low-scattering perovskite thin films. J. Phys. Chem. C *120*, 28933-28938.
26. Hu, H., Ren, Z., Fong, P.W.K., Qin, M., Liu, D., Lei, D., Lu, X., and Li, G. (2019). Room‐temperature meniscus coating of >20% perovskite solar cells: a film formation mechanism investigation. Adv. Funct. Mater. *29*, 1900092.
27. Ding, J., Han, Q., Ge, Q.-Q., Xue, D.-J., Ma, J.-Y., Zhao, B.-Y., Chen, Y.-X., Liu, J., Mitzi, D.B., and Hu, J.-S. (2019). Fully air-bladed high-efficiency perovskite photovoltaics. Joule *3*, 402-416.
28. He, M., Li, B., Cui, X., Jiang, B., He, Y., Chen, Y., O'Neil, D., Szymanski, P., Ei-Sayed, M.A., Huang, J., et al. (2017). Meniscus-assisted solution printing of large-grained perovskite films for high-efficiency solar cells. Nat. Commun. *8*, 16045.
29. Munir, R., Sheikh, A.D., Abdelsamie, M., Hu, H., Yu, L., Zhao, K., Kim, T., Tall, O.E., Li, R., Smilgies, D.M., et al. (2017). Hybrid perovskite thin-film photovoltaics: in situ diagnostics and importance of the precursor solvate phases. Adv. Mater. *29*, 1604113.
30. Li, J., Munir, R., Fan, Y., Niu, T., Liu, Y., Zhong, Y., Yang, Z., Tian, Y., Liu, B., Sun, J., et al. (2018). Phase transition control for high-performance blade-coated perovskite solar cells. Joule *2*, 1313-1330.
31. Hu, H., Singh, M., Wan, X., Tang, J., Chu, C.-W., and Li, G. (2020). Nucleation and crystal growth control for scalable solution-processed organic–inorganic hybrid perovskite solar cells. J. Mater. Chem. A *8*, 1578-1603.
32. Deng, Y., Van Brackle, C.H., Dai, X., Zhao, J., Chen, B., and Huang, J. (2019). Tailoring solvent

coordination for high-speed, room-temperature blading of perovskite photovoltaic films. Sci. Adv. *5*, eaax7537.

33. Wu, W.-Q., Yang, Z., Rudd, P.N., Shao, Y., Dai, X., Wei, H., Zhao, J., Fang, Y., Wang, Q., Liu, Y., et al. (2019). Bilateral alkylamine for suppressing charge recombination and improving stability in blade-coated perovskite solar cells. Sci. Adv. *5*, 8925.
34. Li, X., Dar, M.I., Yi, C., Luo, J., Tschumi, M., Zakeeruddin, S.M., Nazeeruddin, M.K., Han, H., and Gratzel, M. (2015). Improved performance and stability of perovskite solar cells by crystal crosslinking with alkylphosphonic acid omega-ammonium chlorides. Nat. Chem. *7*, 703-711.
35. Zheng, X., Deng, Y., Chen, B., Wei, H., Xiao, X., Fang, Y., Lin, Y., Yu, Z., Liu, Y., Wang, Q., et al. (2018). Dual functions of crystallization control and defect passivation enabled by sulfonic zwitterions for stable and efficient perovskite solar cells. Adv. Mater. *30*, e1803428.
36. Qin, P.L., Yang, G., Ren, Z.W., Cheung, S.H., So, S.K., Chen, L., Hao, J., Hou, J., and Li, G. (2018). Stable and efficient organo-metal halide hybrid perovskite solar cells via pi-conjugated lewis base polymer induced trap passivation and charge extraction. Adv. Mater. *30*, 1706126.
37. Zhang, F., and Zhu, K. (2019). Additive engineering for efficient and stable perovskite solar cells. Adv. Energy Mater. *10*, 1902579.
38. Wu, W.-Q., Wang, Q., Fang, Y., Shao, Y., Tang, S., Deng, Y., Lu, H., Liu, Y., Li, T., Yang, Z., et al. (2018). Molecular doping enabled scalable blading of efficient hole-transport-layer-free perovskite solar cells. Nat. Commun. *9*, 1625.
39. Deng, Y., Zheng, X., Bai, Y., Wang, Q., Zhao, J., and Huang, J. (2018). Surfactant-controlled ink drying enables high-speed deposition of perovskite films for efficient photovoltaic modules. Nat. Energy *3*, 560-566.
40. Pearson, J.R.A. (1958). On convection cells induced by surface tension. J. Fluid Mech. *4*, 489-500.
41. Islam, A., Li, J., Pervaiz, M., Lu, Z.-H., Sain, M., Chen, L., and Ouyang, X. (2019). Zwitterions for organic/perovskite solar cells, light-emitting devices, and lithium ion batteries: recent progress and perspectives. Adv. Energy Mater. *9*, 1803354.
42. Zheng, X., Chen, B., Dai, J., Fang, Y., Bai, Y., Lin, Y., Wei, H., Zeng, Xiao C., and Huang, J. (2017). Defect passivation in hybrid perovskite solar cells using quaternary ammonium halide anions and cations. Nat. Energy *2*, 17102.

43. Bi, D., Li, X., Milic, J.V., Kubicki, D.J., Pellet, N., Luo, J., LaGrange, T., Mettraux, P., Emsley, L., Zakeeruddin, S.M., et al. (2018). Multifunctional molecular modulators for perovskite solar cells with over 20% efficiency and high operational stability. Nat. Commun. *9*, 4482.
44. Conings, B., Babayigit, A., Klug, M.T., Bai, S., Gauquelin, N., Sakai, N., Wang, J.T., Verbeeck, J., Boyen, H.G., and Snaith, H.J. (2016). A universal deposition protocol for planar heterojunction solar cells with high efficiency based on hybrid lead halide perovskite families. Adv. Mater. *28*, 10701-10709.
45. Babayigit, A., D'Haen, J., Boyen, H.-G., and Conings, B. (2018). Gas quenching for perovskite thin film deposition. Joule *2*, 1205-1209.
46. Sept, D., and Tuszyński, J.A. (1994). Inhomogeneous nucleation in first-order phase transitions. Phys. Rev. E *50*, 4906-4910.
47. Dudarev, S.L. (2000). Inhomogeneous nucleation and growth of cavities in irradiated materials. Phys. Rev. B *62*, 9325-9337.
48. Cao, J., Jing, X., Yan, J., Hu, C., Chen, R., Yin, J., Li, J., and Zheng, N. (2016). Identifying the molecular structures of intermediates for optimizing the fabrication of high-quality perovskite films. J. Am. Chem. Soc. *138*, 9919-9926.
49. Hu, Q., Zhao, L., Wu, J., Gao, K., Luo, D., Jiang, Y., Zhang, Z., Zhu, C., Schaible, E., Hexemer, A., et al. (2017). In situ dynamic observations of perovskite crystallisation and microstructure evolution intermediated from [PbI6](4-) cage nanoparticles. Nat. Commun. *8*, 15688.
50. Zhang, K., Wang, Z., Wang, G., Wang, J., Li, Y., Qian, W., Zheng, S., Xiao, S., and Yang, S. (2020). A prenucleation strategy for ambient fabrication of perovskite solar cells with high device performance uniformity. Nat. Commun. *11*, 1006.
51. Qin, M., Tse, K., Lau, T.K., Li, Y., Su, C.J., Yang, G., Chen, J., Zhu, J., Jeng, U.S., Li, G., et al. (2019). Manipulating the mixed-perovskite crystallization pathway unveiled by in situ GIWAXS. Adv. Mater. *31*, 1901284.
52. Ahn, N., Son, D.Y., Jang, I.H., Kang, S.M., Choi, M., and Park, N.G. (2015). Highly reproducible perovskite solar cells with average efficiency of 18.3% and best efficiency of 19.7% fabricated via lewis base adduct of lead(II) iodide. J. Am. Chem. Soc. *137*, 8696-8699.
53. Liu, C., Cheng, Y.B., and Ge, Z. (2020). Understanding of perovskite crystal growth and film formation in scalable deposition processes. Chem. Soc. Rev. *49*, 1653-1687.

54. Lu, J., Jiang, L., Li, W., Li, F., Pai, N.K., Scully, A.D., Tsai, C.-M., Bach, U., Simonov, A.N., Cheng, Y.-B., et al. (2017). Diammonium and monoammonium mixed-organic-cation perovskites for high performance solar cells with improved stability. Adv. Energy Mater. *7*, 1700444.

55. Hoffman, J.M., Strzalka, J., Flanders, N.C., Hadar, I., Cuthriell, S.A., Zhang, Q., Schaller, R.D., Dichtel, W.R., Chen, L.X., and Kanatzidis, M.G. (2020). In situ grazing-incidence wide-angle scattering reveals mechanisms for phase distribution and disorientation in 2D halide perovskite films. Adv. Mater., e2002812.

56. Wang, R., Xue, J., Meng, L., Lee, J.-W., Zhao, Z., Sun, P., Cai, L., Huang, T., Wang, Z., Wang, Z.-K., et al. (2019). Caffeine improves the performance and thermal stability of perovskite solar cells. Joule *3*, 1464-1477.

57. Maiberg, M., Hölscher, T., Zahedi-Azad, S., and Scheer, R. (2015). Theoretical study of time-resolved luminescence in semiconductors. III. Trap states in the band gap. J. Appl. Phys. *118*, 105701.

58. Wu, B., Nguyen, H.T., Ku, Z., Han, G., Giovanni, D., Mathews, N., Fan, H.J., and Sum, T.C. (2016). Discerning the surface and bulk recombination kinetics of organic-inorganic halide perovskite single crystals. Adv. Energy Mater. *6*, 1600551.

59. Yamada, Y., Nakamura, T., Endo, M., Wakamiya, A., and Kanemitsu, Y. (2014). Photocarrier recombination dynamics in perovskite CH3NH3PbI3 for solar cell applications. J. Am. Chem. Soc. *136*, 11610-11613.

60. Bi, D., Yi, C., Luo, J., Décoppet, J.-D., Zhang, F., Zakeeruddin, Shaik M., Li, X., Hagfeldt, A., and Grätzel, M. (2016). Polymer-templated nucleation and crystal growth of perovskite films for solar cells with efficiency greater than 21%. Nat. Energy *1*, 16142.

61. Zhou, W., Li, D., Xiao, Z., Wen, Z., Zhang, M., Hu, W., Wu, X., Wang, M., Zhang, W.H., Lu, Y., et al. (2019). Zwitterion coordination induced highly orientational order of CH3NH3PbI3 perovskite film delivers a high open circuit voltage exceeding 1.2 V. Adv. Funct. Mater. *29*, 1901026.

62. Tai, Q., Guo, X., Tang, G., You, P., Ng, T.W., Shen, D., Cao, J., Liu, C.K., Wang, N., Zhu, Y., et al. (2019). Antioxidant grain passivation for air-stable tin-based perovskite solar cells. Angew. Chem. Int. Ed. Engl. *58*, 806-810.

63. Wang, Q., Zheng, X., Deng, Y., Zhao, J., Chen, Z., and Huang, J. (2017). Stabilizing the α-phase of CsPbI3 perovskite by sulfobetaine zwitterions in one-step spin-coating films. Joule *1*, 371-382.

64. Murgatroyd, P.N. (1970). Theory of space-charge-limited current enhanced by Frenkel effect. J. Phys. D: Appl. Phys. *3*, 151-156.

65. Samiee, M., Konduri, S., Ganapathy, B., Kottokkaran, R., Abbas, H.A., Kitahara, A., Joshi, P., Zhang, L., Noack, M., and Dalal, V. (2014). Defect density and dielectric constant in perovskite solar cells. Appl. Phys. Lett. *105*, 153502.

66. Peng, J., Chen, Y., Zheng, K., Pullerits, T., and Liang, Z. (2017). Insights into charge carrier dynamics in organo-metal halide perovskites: from neat films to solar cells. Chem. Soc. Rev. *46*, 5714-5729.

67. Jiang, Q., Zhao, Y., Zhang, X., Yang, X., Chen, Y., Chu, Z., Ye, Q., Li, X., Yin, Z., and You, J. (2019). Surface passivation of perovskite film for efficient solar cells. Nat. Photonics *13*, 460-466.

68. Tress, W., Marinova, N., Inganäs, O., Nazeeruddin, M.K., Zakeeruddin, S.M., and Graetzel, M. (2015). Predicting the open-circuit voltage of CH3NH3PbI3 perovskite solar cells using electroluminescence and photovoltaic quantum efficiency spectra: the role of radiative and non-radiative recombination. Adv. Energy Mater. *5*, 1400812.

69. Rau, U. (2007). Reciprocity relation between photovoltaic quantum efficiency and electroluminescent emission of solar cells. Phys. Rev. B *76*, 085303.

70. Yao, J., Kirchartz, T., Vezie, M.S., Faist, M.A., Gong, W., He, Z., Wu, H., Troughton, J., Watson, T., Bryant, D., et al. (2015). Quantifying losses in open-circuit voltage in solution-processable solar cells. Phys. Rev. Appl. *4*, 014020.

71. Luo, D., Su, R., Zhang, W., Gong, Q., and Zhu, R. (2020). Minimizing non-radiative recombination losses in perovskite solar cells. Nat. Rev. Mater. *5*, 44-60.

72. Duan, C., Cui, J., Zhang, M., Han, Y., Yang, S., Zhao, H., Bian, H., Yao, J., Zhao, K., Liu, Z., et al. (2020). Precursor engineering for ambient‐compatible antisolvent‐free fabrication of high‐efficiency CsPbI2Br perovskite solar cells. Adv. Energy Mater. *10*, 2000691.

73. Zhang, M., Chen, Q., Xue, R., Zhan, Y., Wang, C., Lai, J., Yang, J., Lin, H., Yao, J., Li, Y., et al. (2019). Reconfiguration of interfacial energy band structure for high-performance inverted

structure perovskite solar cells. Nat. Commun. *10*, 4593.

74. Heo, J.H., Song, D.H., Han, H.J., Kim, S.Y., Kim, J.H., Kim, D., Shin, H.W., Ahn, T.K., Wolf, C., Lee, T.W., et al. (2015). Planar CH3NH3PbI3 perovskite solar cells with constant 17.2% average power conversion efficiency irrespective of the scan rate. Adv. Mater. *27*, 3424-3430.
75. Li, N., Tao, S., Chen, Y., Niu, X., Onwudinanti, C.K., Hu, C., Qiu, Z., Xu, Z., Zheng, G., Wang, L., et al. (2019). Cation and anion immobilization through chemical bonding enhancement with fluorides for stable halide perovskite solar cells. Nat. Energy *4*, 408-415.
76. Saliba, M., Matsui, T., Seo, J.Y., Domanski, K., Correa-Baena, J.P., Nazeeruddin, M.K., Zakeeruddin, S.M., Tress, W., Abate, A., Hagfeldt, A., et al. (2016). Cesium-containing triple cation perovskite solar cells: improved stability, reproducibility and high efficiency. Energy Environ. Sci. *9*, 1989-1997.
77. Wu, J., Cui, Y., Yu, B., Liu, K., Li, Y., Li, H., Shi, J., Wu, H., Luo, Y., Li, D., et al. (2019). A simple way to simultaneously release the interface stress and realize the inner encapsulation for highly efficient and stable perovskite solar cells. Adv. Funct. Mater. *29*, 1905336.
78. Christians, J.A., Miranda Herrera, P.A., and Kamat, P.V. (2015). Transformation of the excited state and photovoltaic efficiency of CH3NH3PbI3 perovskite upon controlled exposure to humidified air. J. Am. Chem. Soc. *137*, 1530-1538.

Figure 1. Perovskite Film Deposition and Morphology

(A) Schematic illustration of the zwitterionic surfactant assisted meniscus coating at room temperature.

(B) Schematic illustration of the coordinate interaction between TAH and charged defects at perovskite surface and GBs and spontaneous formation of moisture barrier.

(C) Photographs of the blade-coated perovskite films with different amount of TAH on PTAA coated ITO substrates.

(D) Contact angles of the corresponding perovskite ink droplets on PTAA coated ITO substrates.

(E) ToF-SIMS depth profile analysis in the TAH incorporated perovskite film.

Figure 2. Crystallization Kinetics of the Intermediate Complex and Perovskite

(A) In-situ GIWAXS intensity profiles measured within 100 frames during the drying process of perovskite inks without (left) and with 0.1 wt% TAH (right).

(B) In-situ GIWAXS false-color intensity maps versus *q* and frame numbers during the drying process of perovskite inks without (left) and with 0.1 wt% TAH (right).

(C) In-situ UV-vis absorption spectra as a function of annealing time for the perovskite without and with 0.1 wt% TAH at 100°C.

(D) UV-vis absorption intensity at the wavelength of 550 nm as a function of annealing time for the perovskite without and with 0.1 wt% TAH.

Figure 3. Perovskite Crystallization and Orientation

(A) XRD patterns of the annealed perovskite films incorporated with different amount of TAH.

(B) 2D GIWAXS patterns of the pristine (left) and TAH incorporated perovskites (right) at upper surface (α_i = 0.2°) and in the bulk (α_i = 1°).

(C) The polar intensity profiles along the (110) ring in the range of q = 0.95-1.05 $Å^{-1}$ from 2D GIWAXS patterns of the pristine and TAH incorporated perovskites in the bulk (α_i = 1°).

Figure 4. Charged Defects Passivation

(A) Steady-state PL spectra of the perovskite films with different amount of TAH. All samples were prepared on quartz substrates with the excitation at 636.2 nm.

(B) TRPL decays of the perovskite films with different amount of TAH. All samples were prepared on quartz substrates, excited with a 636.2 nm picosecond pulsed laser.

(C) Excitation fluence dependence of the PL lifetime in the TAH incorporated perovskite film. The initial density of photogenerated carriers was also calculated under different excitation fluence.

(D) XPS Pb 4f spectra of the pristine and 0.1 wt% TAH incorporated perovskite films.

(E) FITR spectra of the pure TAH, pristine perovskite, and TAH based perovskite films.

(F) Dark *J*-*V* curves of the electron-only devices based on pristine and TAH incorporated perovskite films. Inset: structure of the electron-only device.

Figure 5. Perovskite Solar Cells Performance

(A) Schematic device architecture of the inverted p-i-n PSCs.

(B) Energy levels diagrams of corresponding components in the inverted p-i-n PSCs

(C) *J-V* curves of the best-performance control and TAH based devices with p-i-n structure.

(D) EQE spectra and integrated J_{SC} values for the control and TAH based devices.

(E) EL spectra for the TAH based device under voltage bias from 1.2 to 1.8 V. Inset: a photograph showing a TAH based PSC operating as a LED (active area: 0.04 cm^2) with visible red emission.

(F) EQE_{EL} as a function of the applied voltage bias for the control and TAH based PSCs when operating as LEDs.

(G) Mott–Schottky plots in the control and TAH based devices.

(H) N_t distribution as a function of defect energy level E_ω for the control and TAH based devices, as measured in TAS method.

(I) *J-V* curves of the best-performance TAH based PSCs with 0.04 and 0.8 cm^2 active area in the conventional n-i-p structure. Inset: a photograph showing a 0.8 cm^2 device.

Figure 6. Water-Resistant Perovskite Films and Device Stability

(A) Dynamic dissolving process of a water droplet on the surface of pristine and TAH incorporated perovskite films.

(B) Ambient stability of the unencapsulated devices shelved under 25±5°C and 20±5% RH. Data were represented as the mean value and the standard deviation from 10 samples in each condition.

(C) Thermal stability of the unencapsulated devices at 80±5°C in nitrogen atmosphere. Data were represented as the mean value and the standard deviation from 5 samples in each condition.

(D) Light stability of the encapsulated devices exposed under continuous 0.7 sun illumination at 40±5°C and 50±5% RH. Data were represented as the mean value and the standard deviation from 5 samples in each condition.

Table 1. Photovoltaic parameters of the blade-coated inverted p-i-n PSCs incorporated with different amount of TAH

TAH concentration (wt%)	V_{OC} (V)	J_{SC}[a] (mA cm^{-2})	FF (%)	PCE (%)	
				Average[b]	Best
w/o	1.067	23.27	77.90	18.38 ± 0.56	19.34
0.02	1.088	23.52	79.12	19.48 ± 0.50	20.24
0.05	1.120	23.85	80.14	20.57 ± 0.43	21.41
0.1	1.126	24.13	81.22	21.18 ± 0.50	22.07
0.2	1.131	23.74	79.33	20.52 ± 0.37	21.30

[a]AR MgF_2 films were deposited on the incident side of ITO/glass substrate.

[b]Average value and standard deviation were calculated from 20 devices.

Click here to access/download;Figure;Figure 1.tif

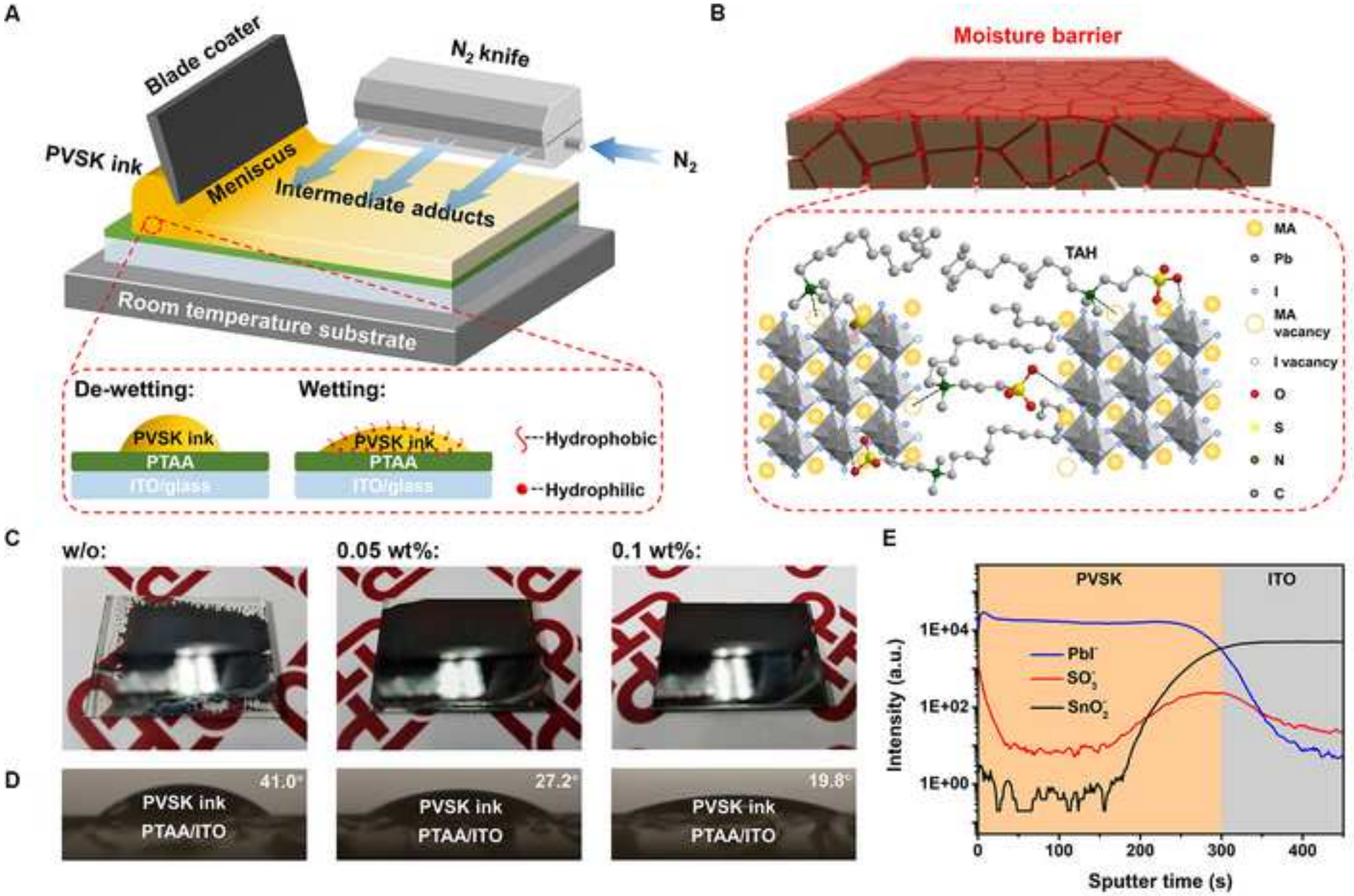

Figure 2

Click here to access/download;Figure;Figure 2.tif

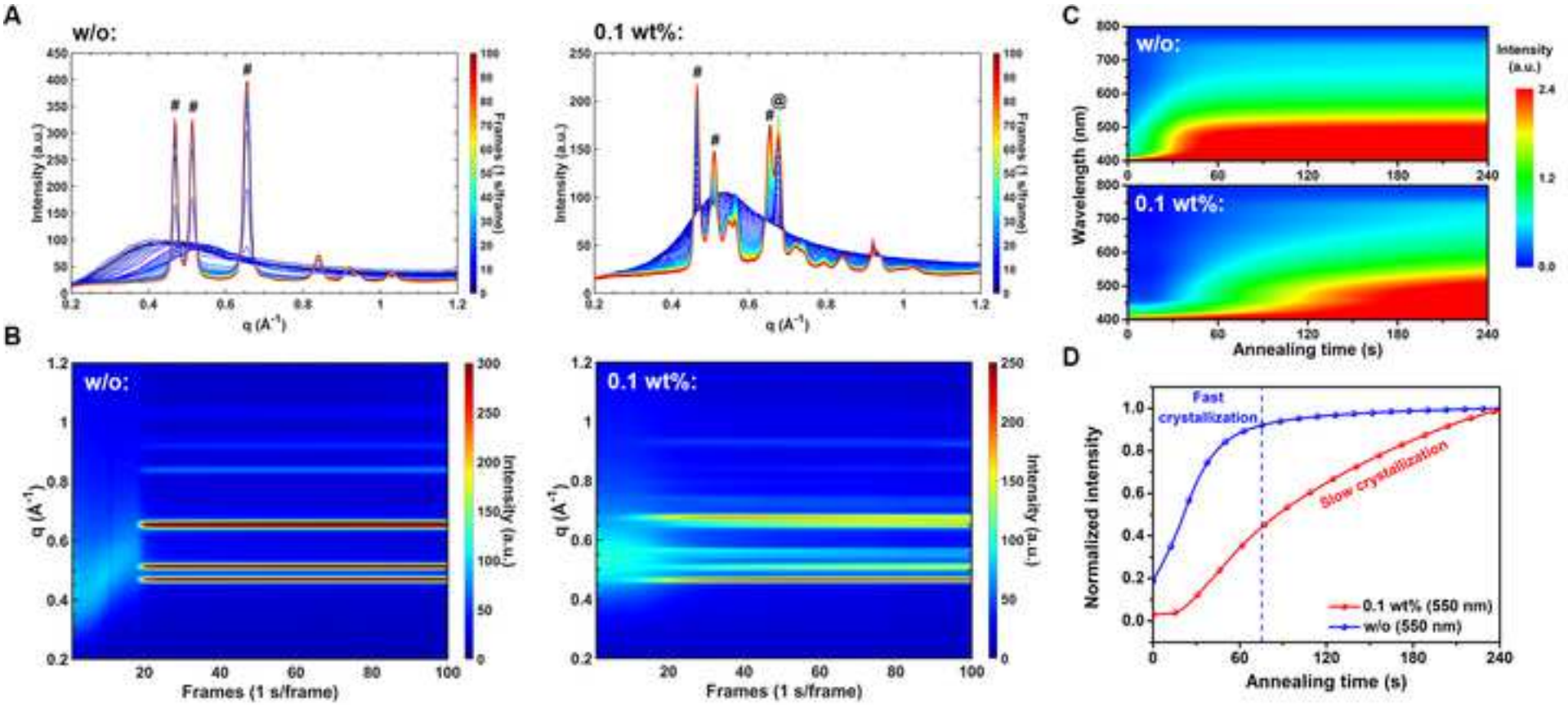

Figure 3

Click here to access/download;Figure;Figure 3.tif

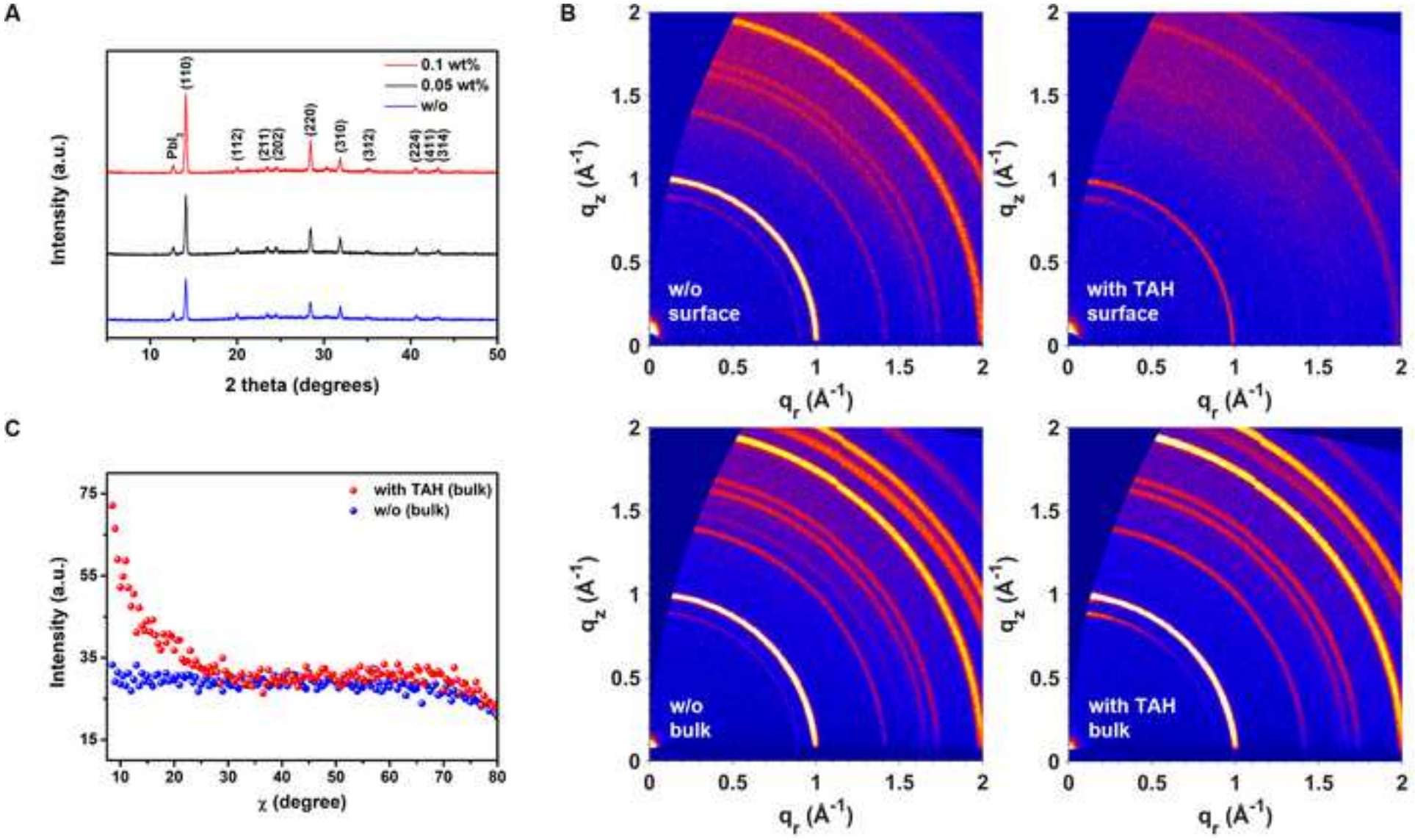

Figure 4

Click here to access/download;Figure;Figure 4.tif

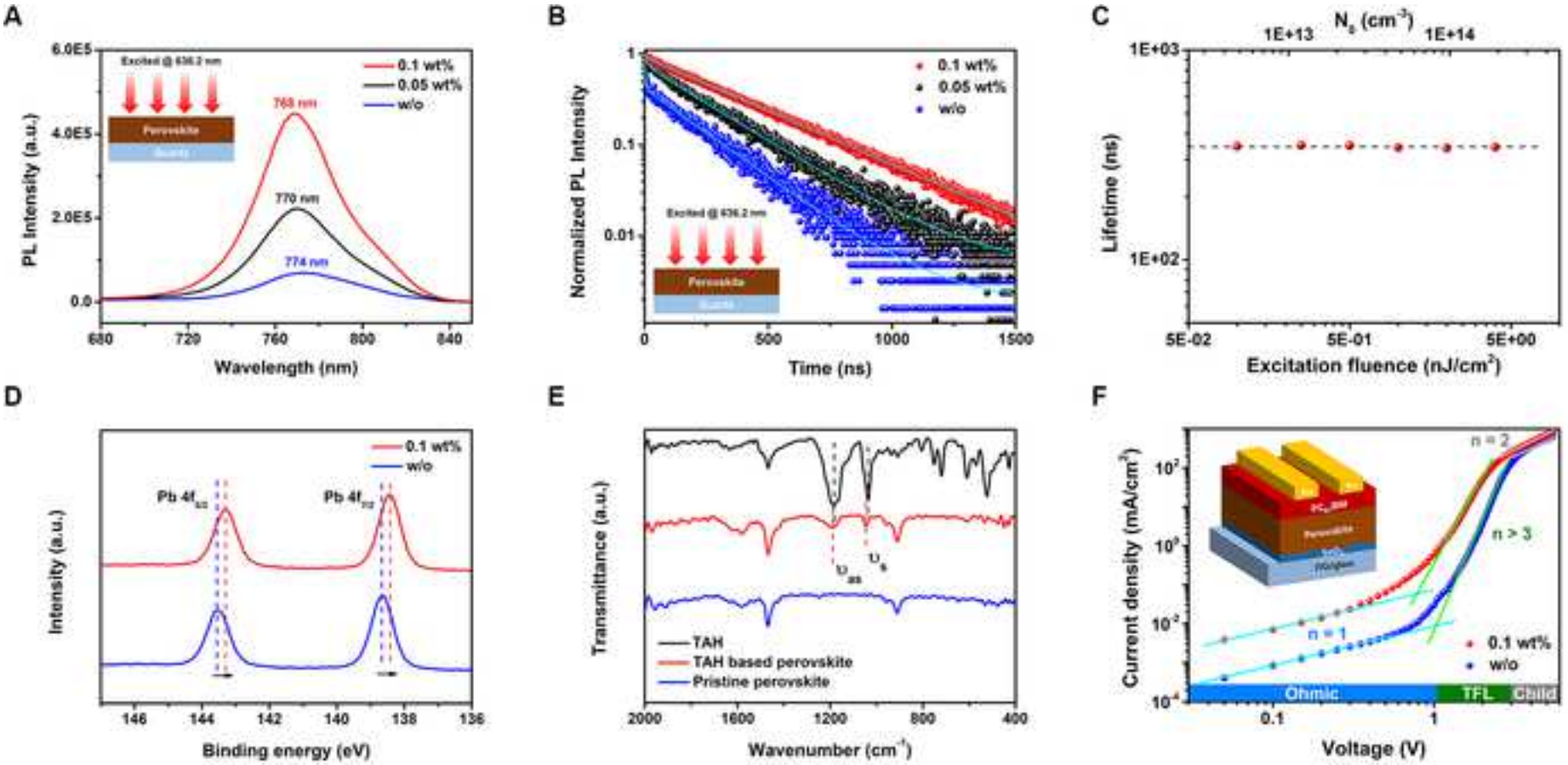

Figure 5

Click here to access/download;Figure;Figure 5.tif

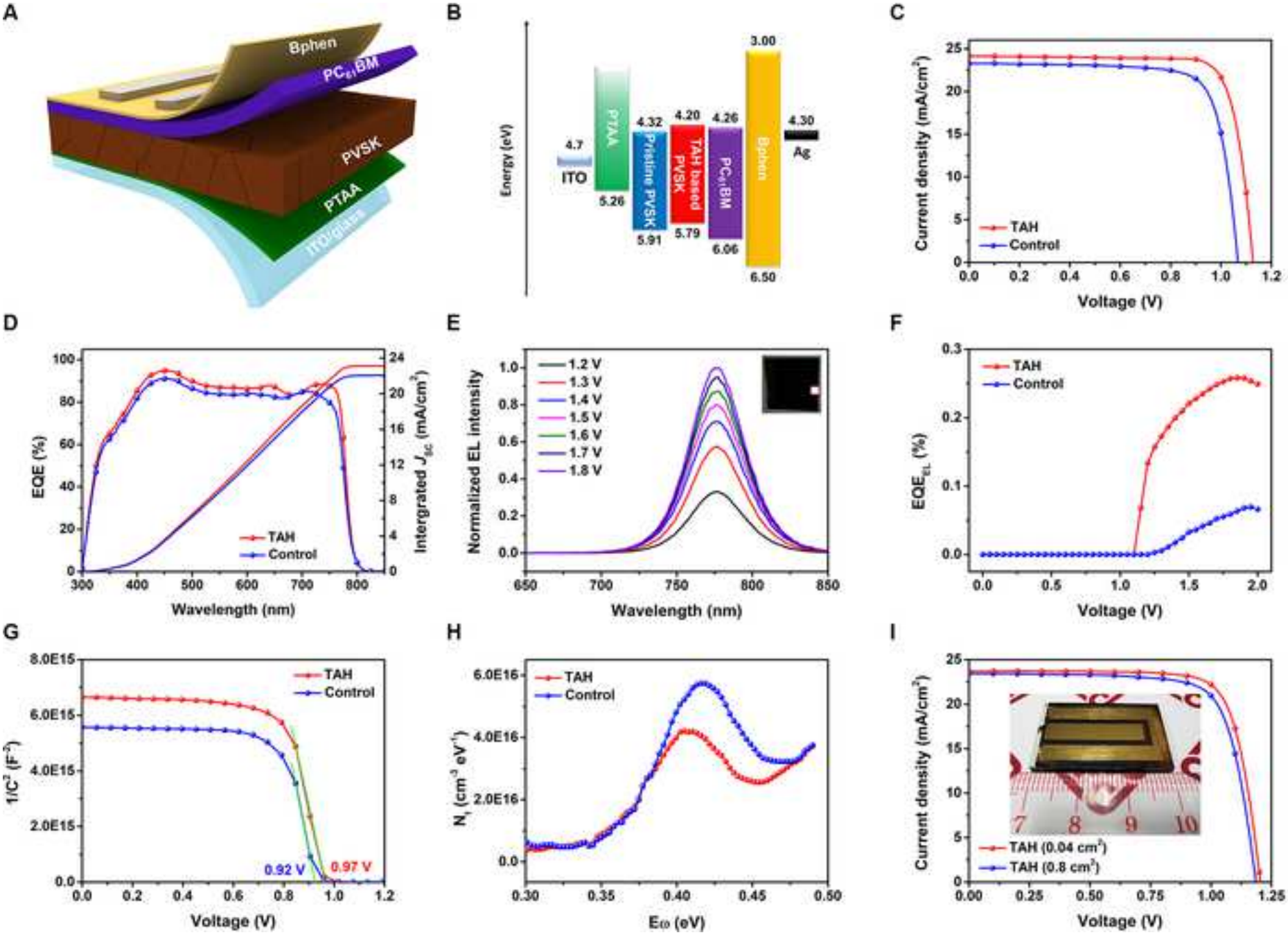

Figure 6

Click here to access/download;Figure;Figure 6.tif

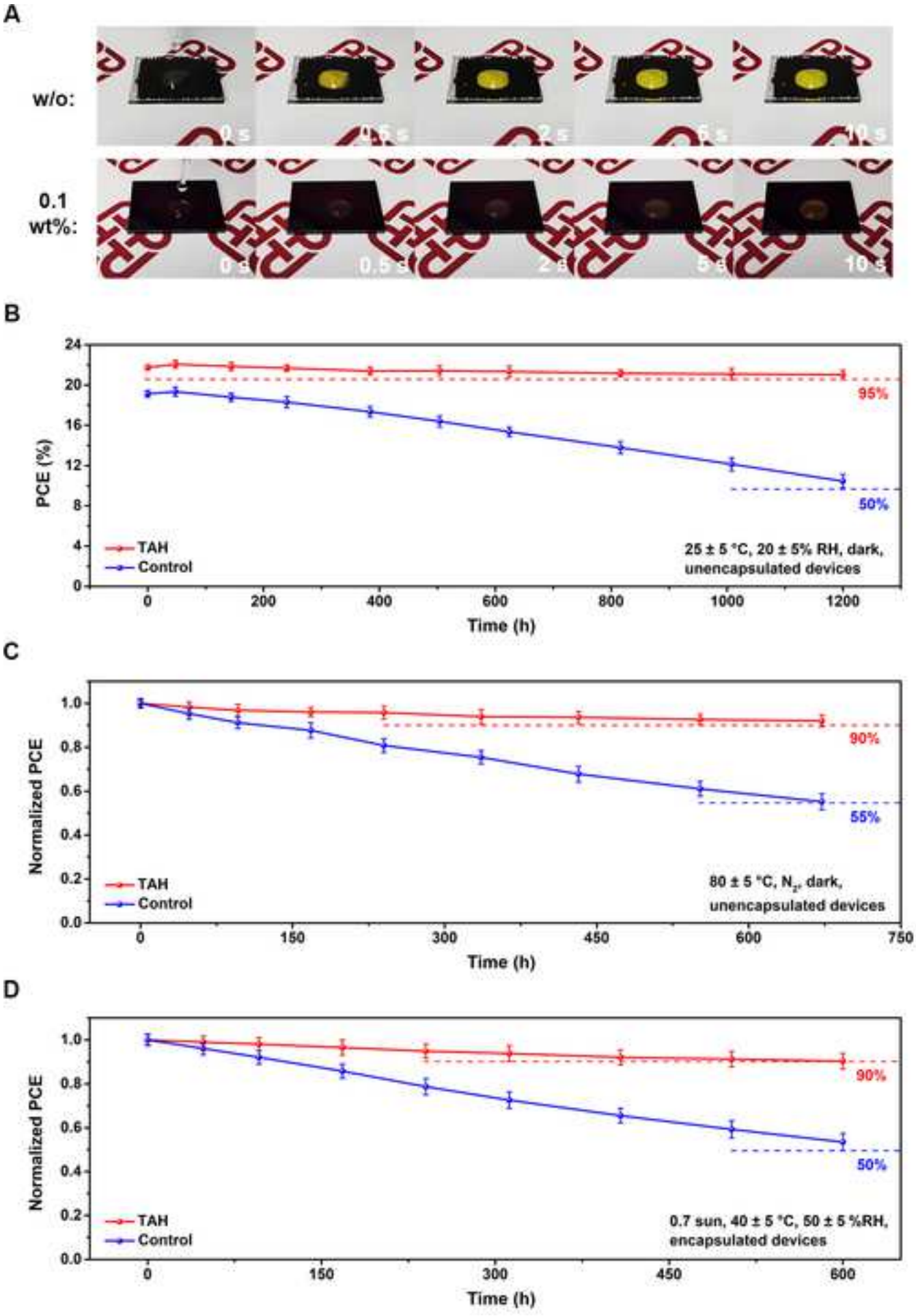

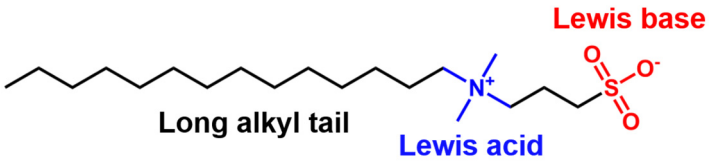

Figure S1. The molecular structure of TAH.

Figure S2. Photographs of the as-cast intermediate films with different amount of TAH before thermal annealing.

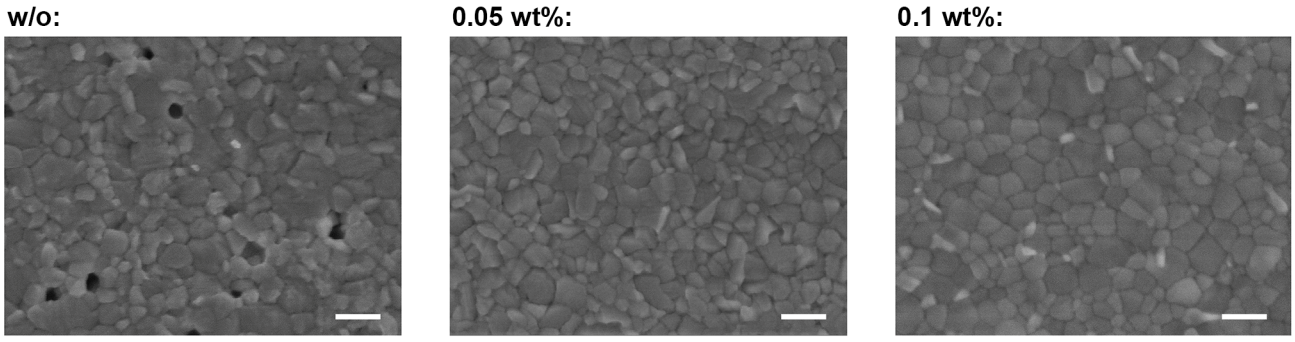

Figure S3. SEM images of the blade-coated perovskite films with different amount of TAH on PTAA coated ITO substrate. Scale bar: 500 nm.

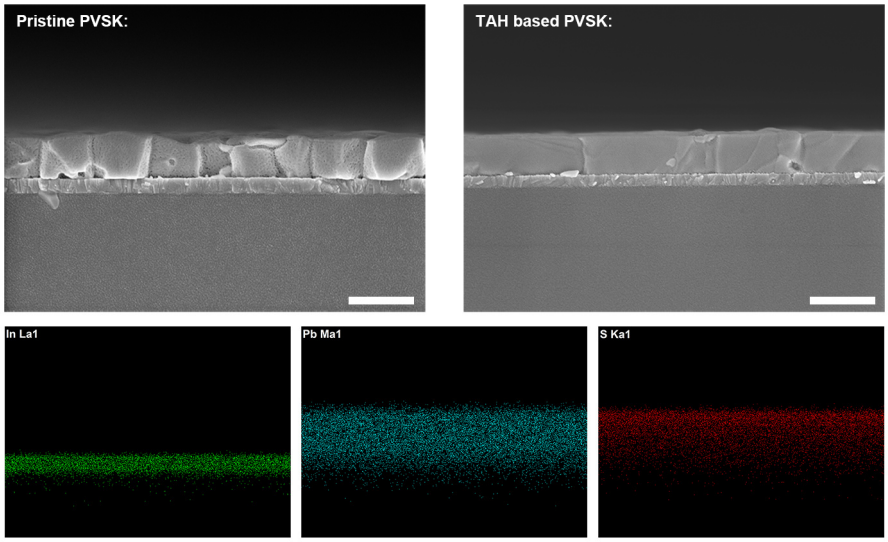

Figure S4. Cross-sectional SEM images of the pristine and TAH based perovskite films blade-coated on PTAA/ITO substrate and corresponding EDX mapping. Scale bar: 500 nm.

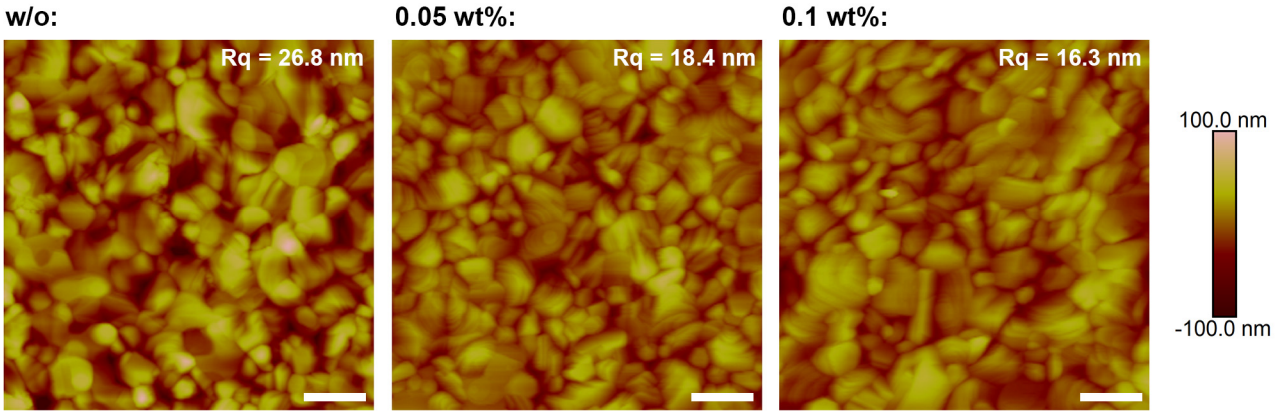

Figure S5. AFM height images of the blade-coated perovskite films with different amount of TAH. Scale bar: 500 nm.

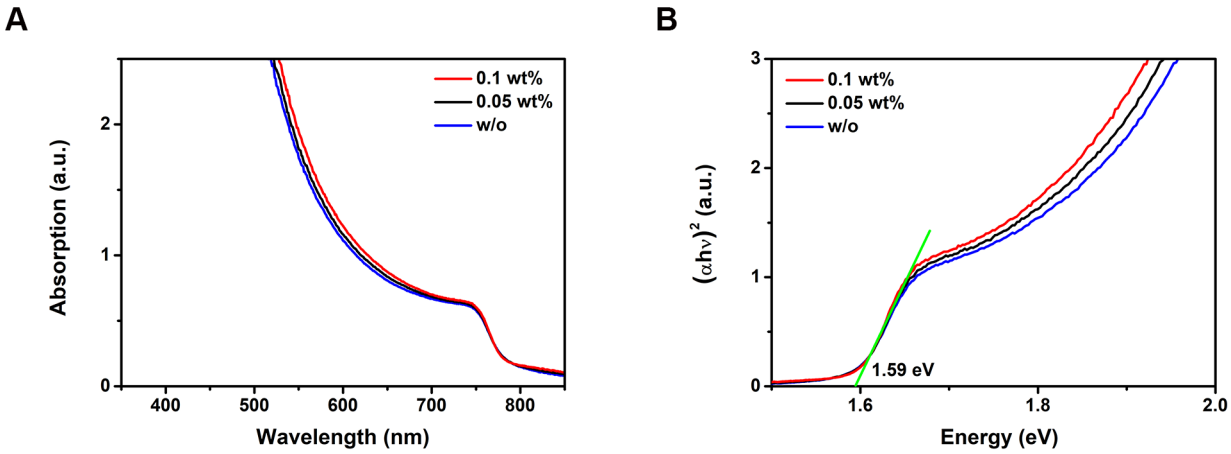

Figure S6. (A) UV-vis absorption spectra of the perovskite films with different amount of TAH. (B) Tauc plots as a function of $(\alpha h\upsilon)^2$ versus energy for the respective perovskite films. The bandgap can be determined via linear extrapolation of the leading edges of the $(\alpha h\upsilon)^2$ curve to the base line

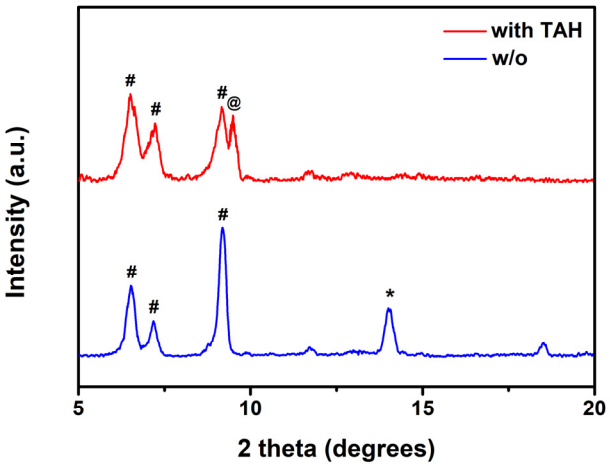

Figure S7. XRD patterns of the as-cast pristine and TAH incorporated perovskite films before thermal annealing.

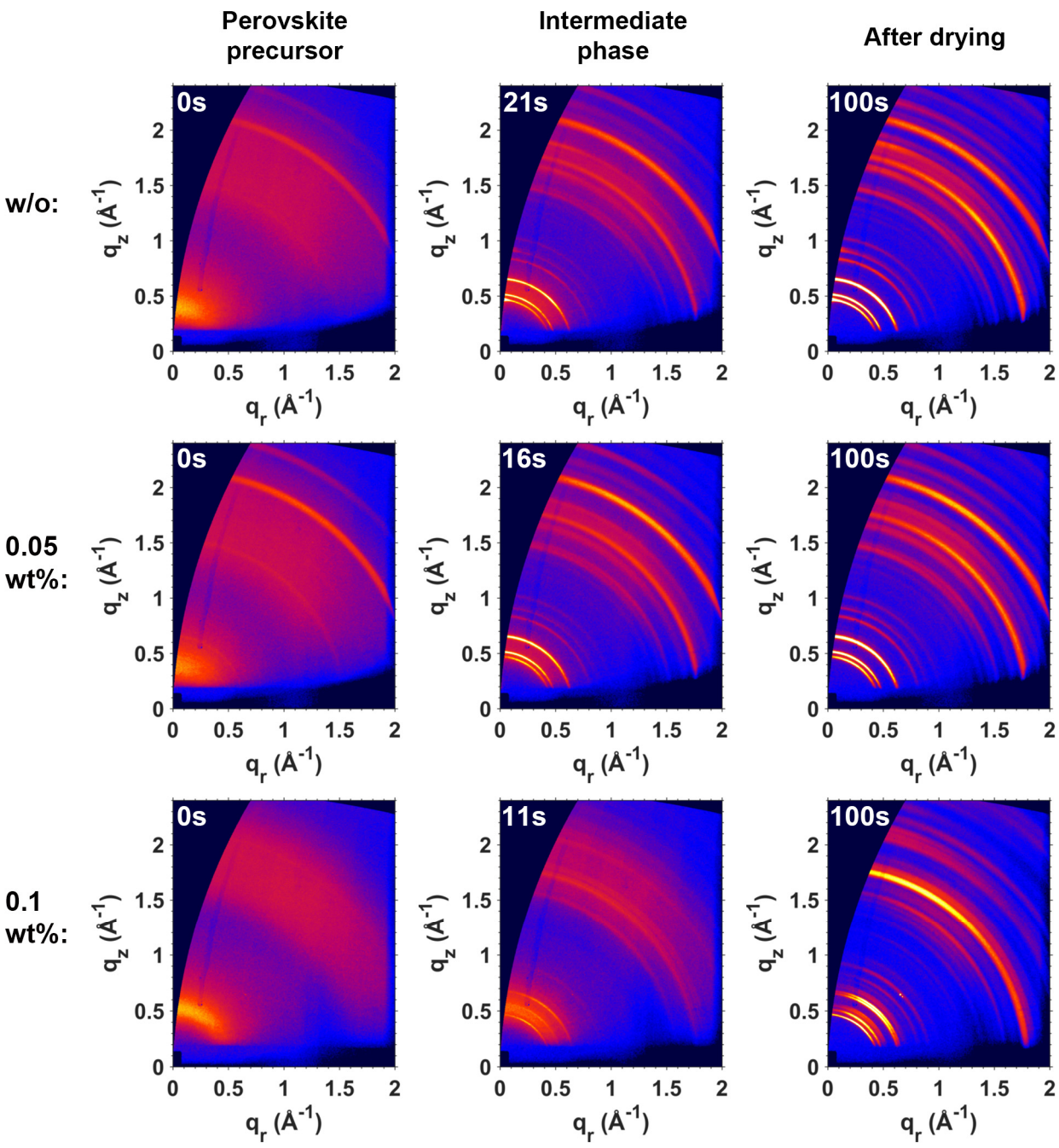

Figure S8. 2D GIWAXS patterns of the respective perovskite inks with different amount of TAH at different crystallization stages versus drying time.

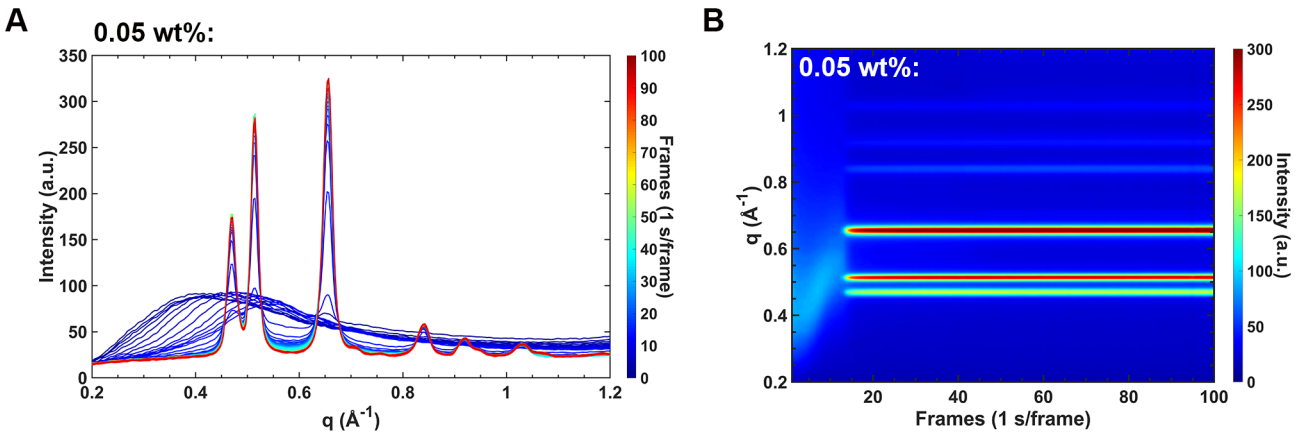

Figure S9. (A) In-situ GIWAXS intensity profile and (B) the corresponding false-color intensity map versus *q* and frame numbers during the drying process of the perovskite ink with 0.05 wt% TAH.

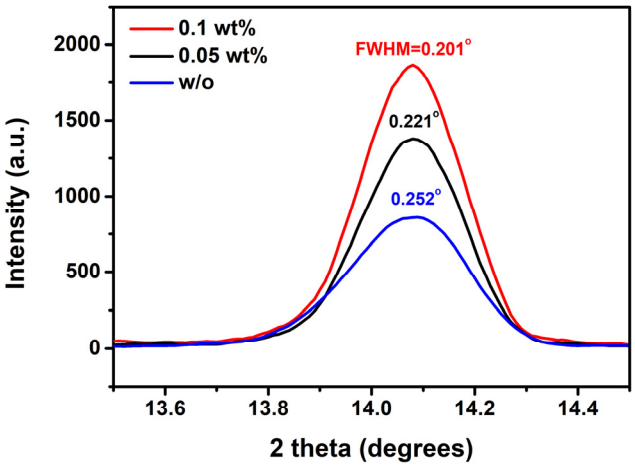

Figure S10. Full width at half maximum (FWHM) of (110) peak in the annealed perovskite films with different amount of TAH.

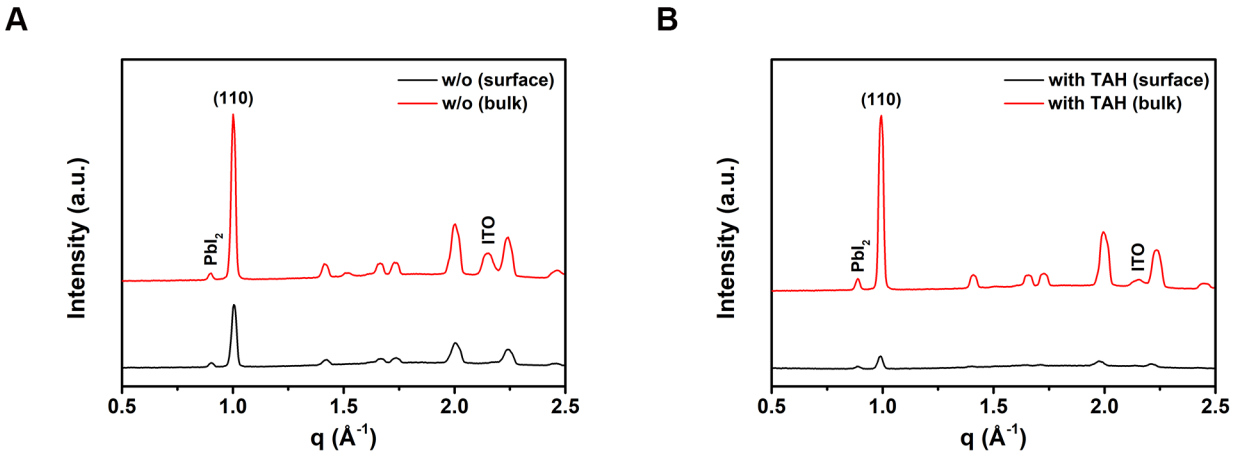

Figure S11. GIWAXS intensity profiles of (A) the pristine and (B) TAH incorporated perovskite films at upper surface (black curve, α_i = 0.2°) and in the bulk (red curve, α_i = 1°) respectively.

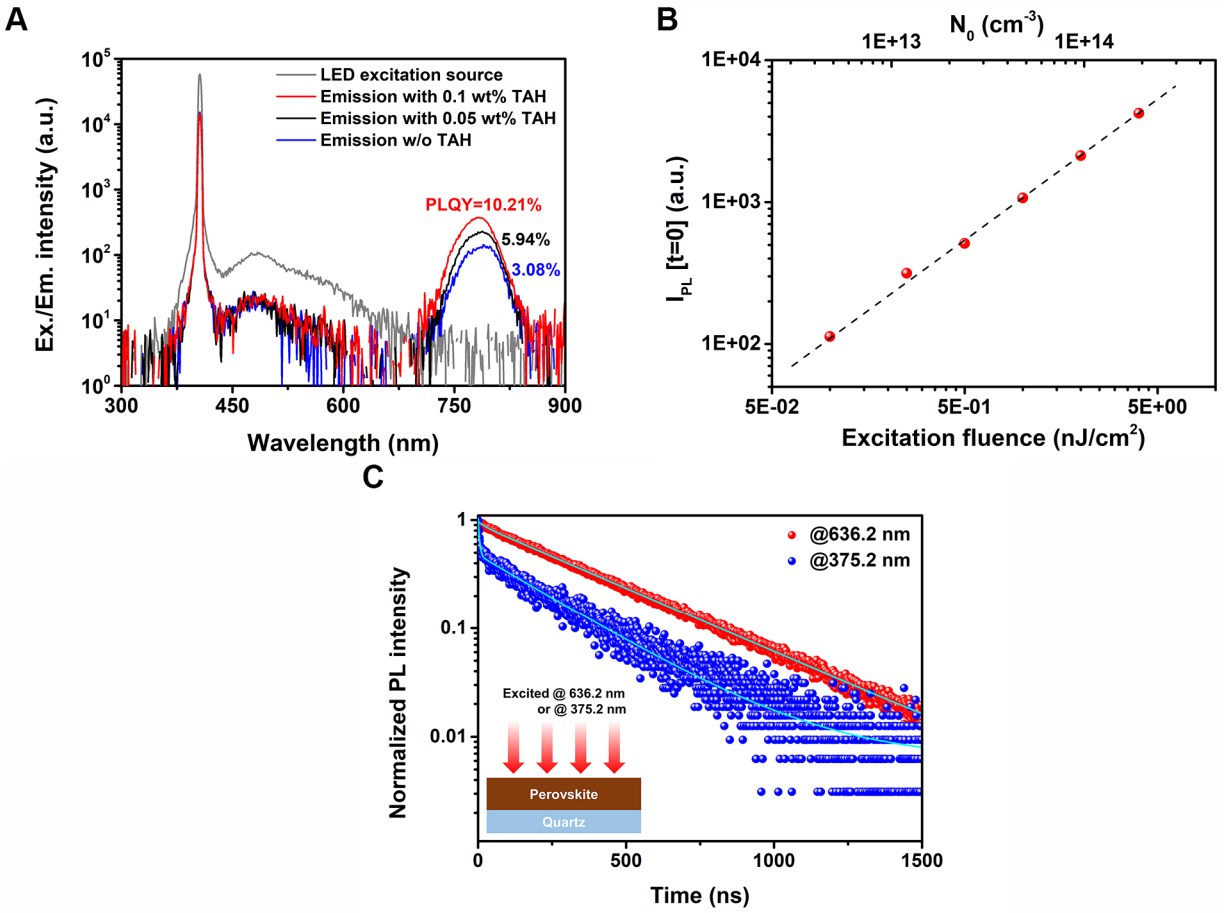

Figure S12. (A) PLQYs of the perovskite films with different amount of TAH. (B) Excitation fluence dependence of the initial PL intensity just after the excitation in the TAH incorporated perovskite film. The initial density of photogenerated carriers was also calculated under different excitation fluence. (C) TRPL decays in the TAH incorporated perovskite with the excitation at 636.2 and 375.2 nm respectively.

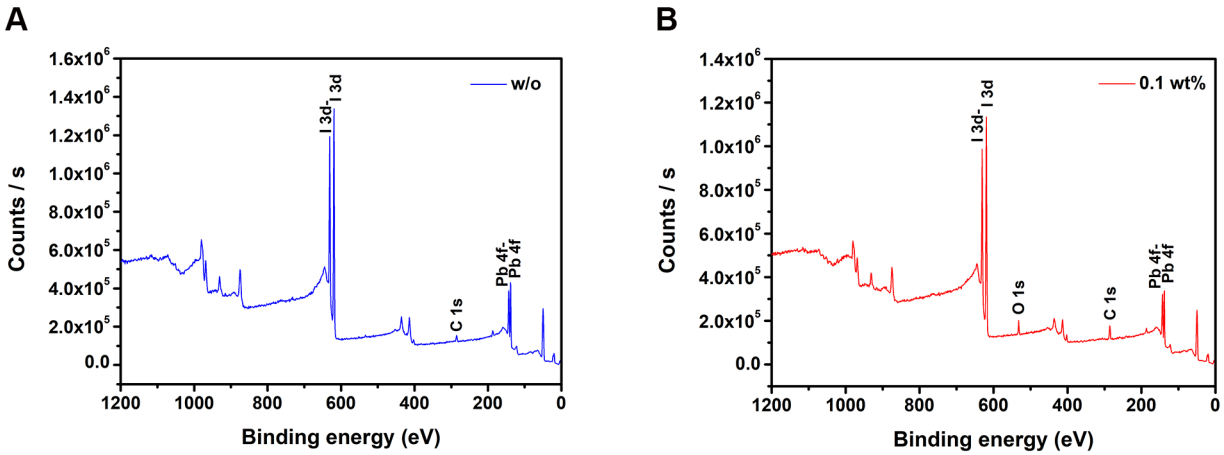

Figure S13. XPS survey for (A) the pristine and (B) 0.1 wt% TAH incorporated perovskite films.

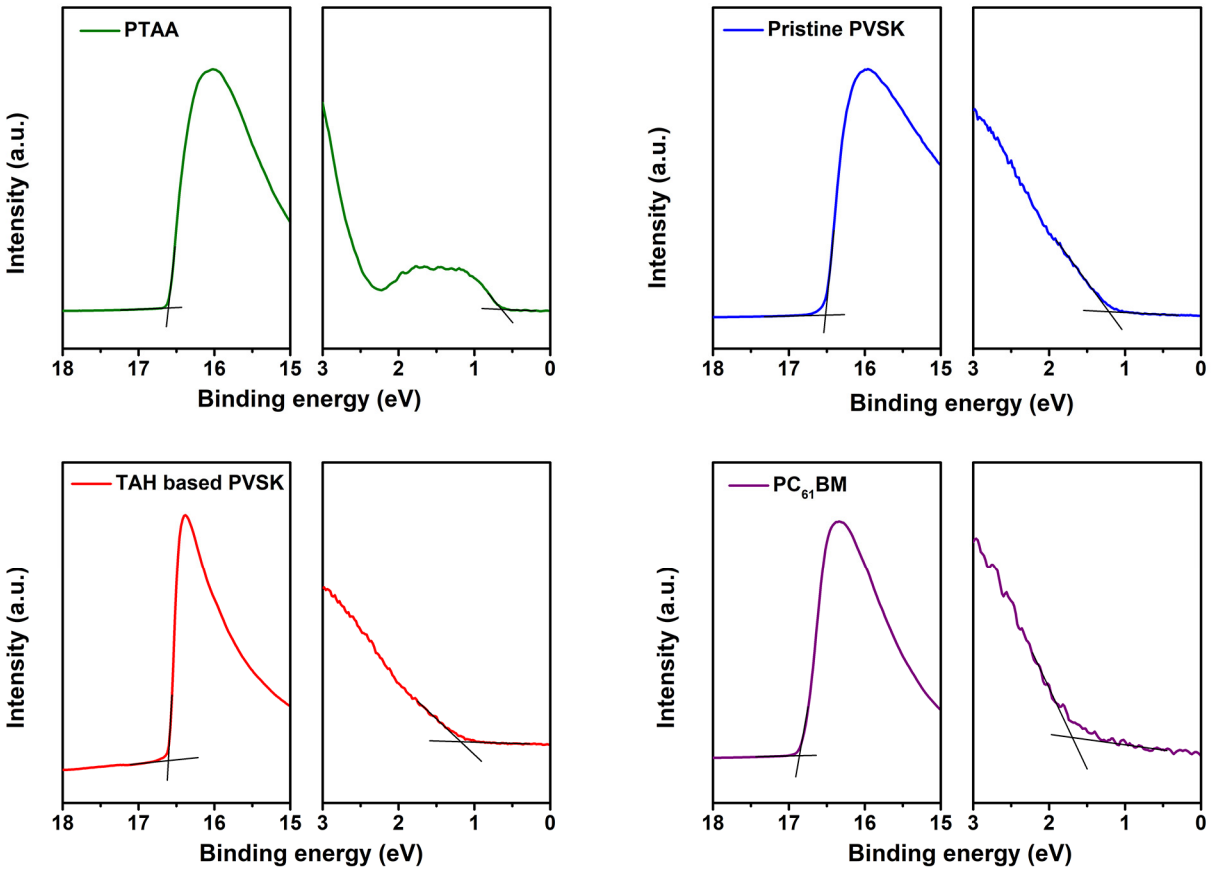

Figure S14. UPS spectra of PTAA, pristine $MAPbI_3$, TAH based $MAPbI_3$ and $PC_{61}BM$ respectively.

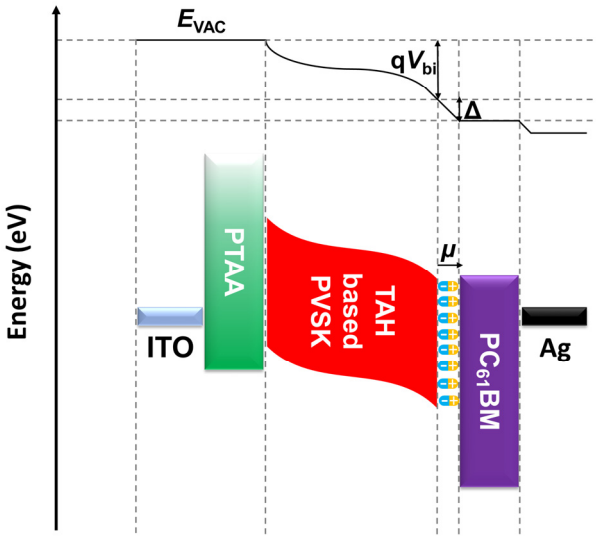

Figure S15. Energy band structure of a complete p-i-n structured PSCs under short-circuit condition and vacuum level offset due to the interfacial dipole.

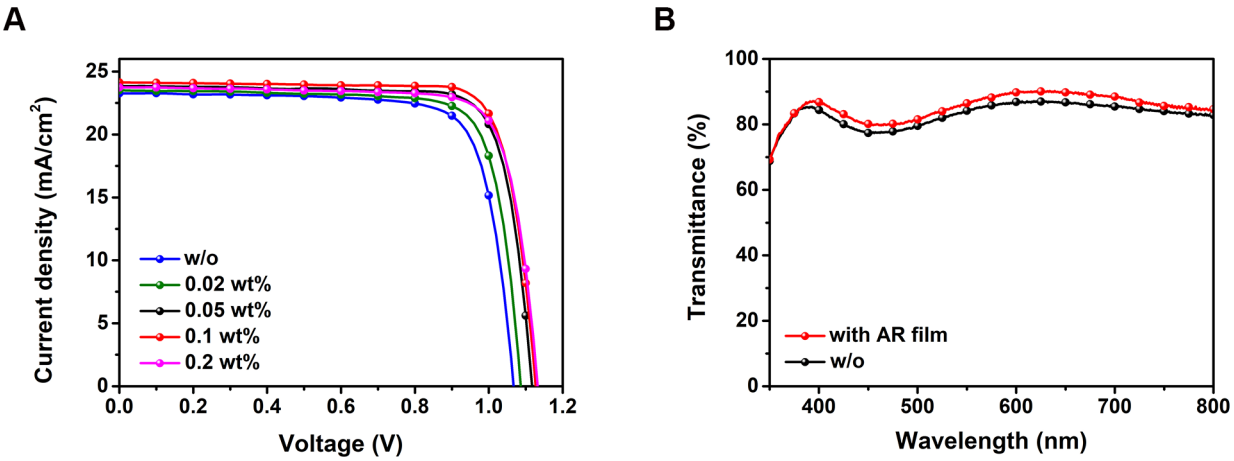

Figure S16. (A) *J-V* curves of the best performance TAH based devices under different concentration. (B) Transmittance of the ITO/glass substrates with and without AR film.

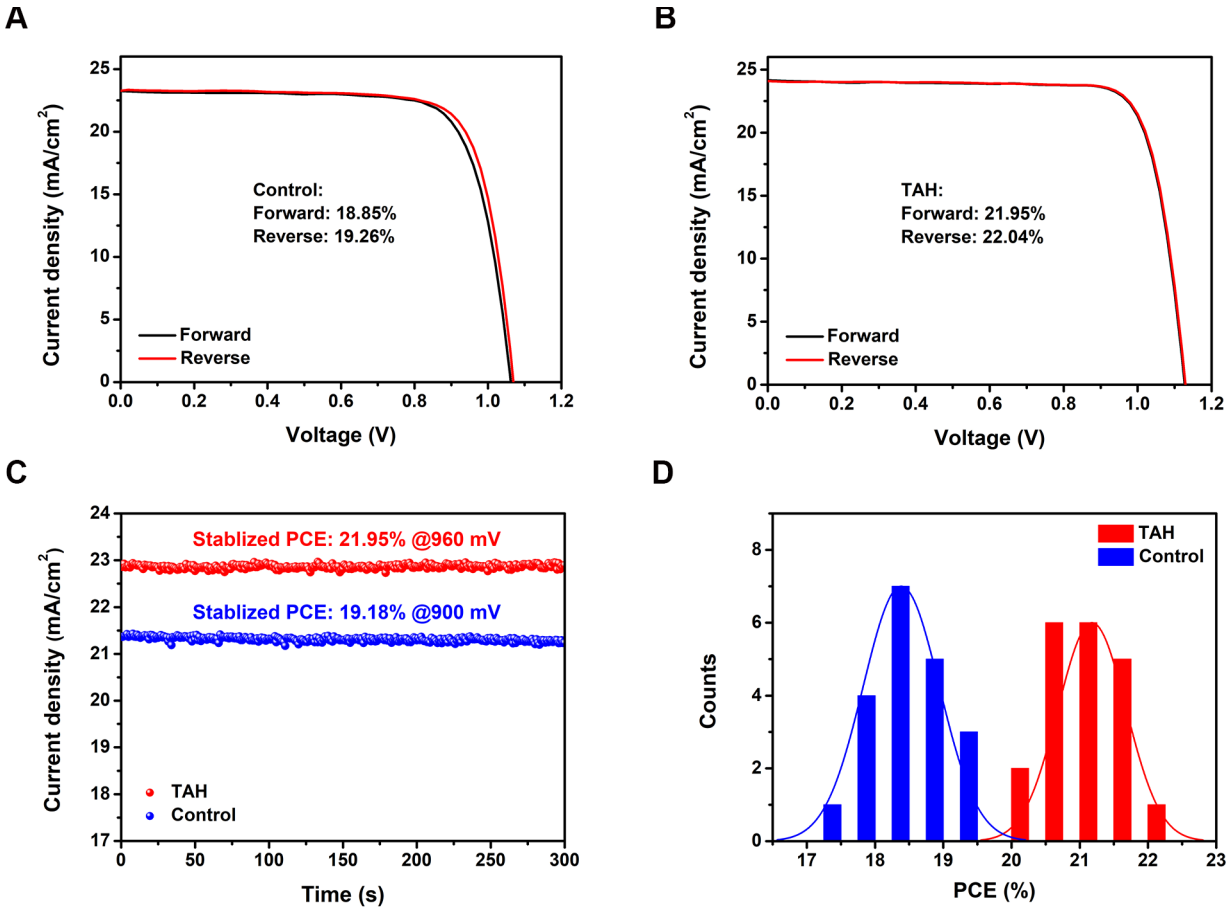

Figure S17. Hysteresis effect in *J-V* curves under different scanning directions for the representative (A) control and (B) TAH based device. (C) Steady-state photocurrent outputs and stabilized PCEs under MPP for the control and TAH based devices. (D) PCEs histogram of 20 control and TAH based devices.

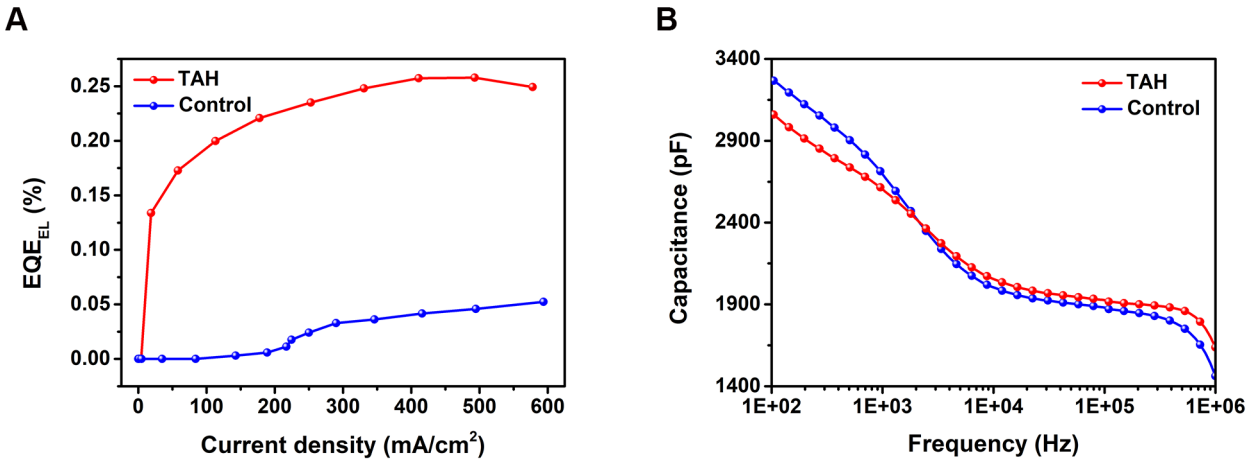

Figure S18. (A) EQE_{EL} as a function of the driving current density for the control and TAH based PSCs when operating as LEDs. (B) Capacitance spectra as a function of AC frequency for the control and TAH based devices.

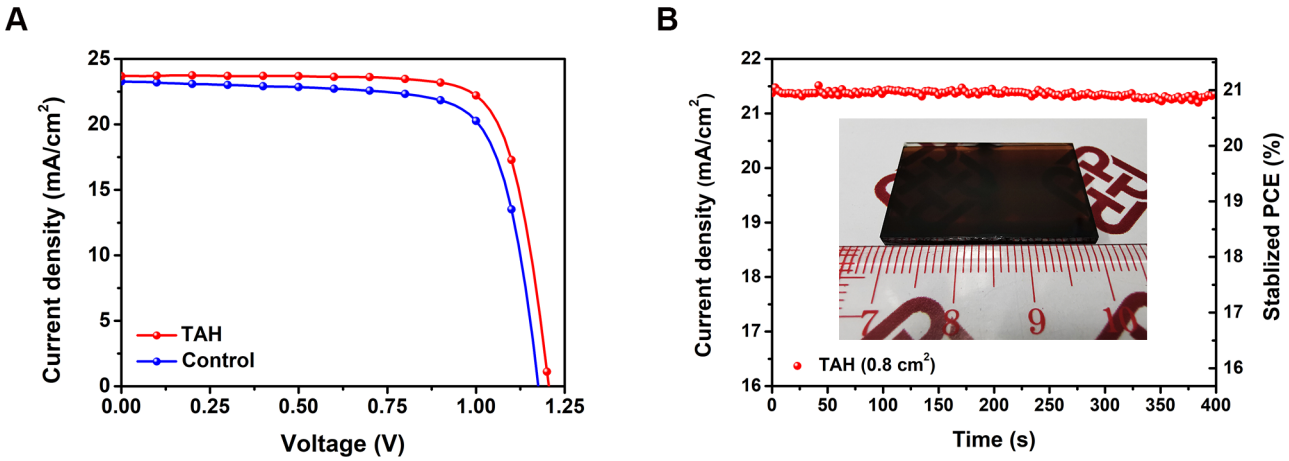

Figure S19. (A) *J-V* curves of the best-performance control and TAH based devices in conventional n-i-p architecture (0.04 cm^2 active area). (B) Steady-state photocurrent output and stabilized PCE under MPP at 0.98 V bias for the TAH based n-i-p device (0.8 cm^2 active area). Inset: a photograph showing a blade-coated perovskite film on FTO substrate with a dimension of 3 cm × 2 cm.

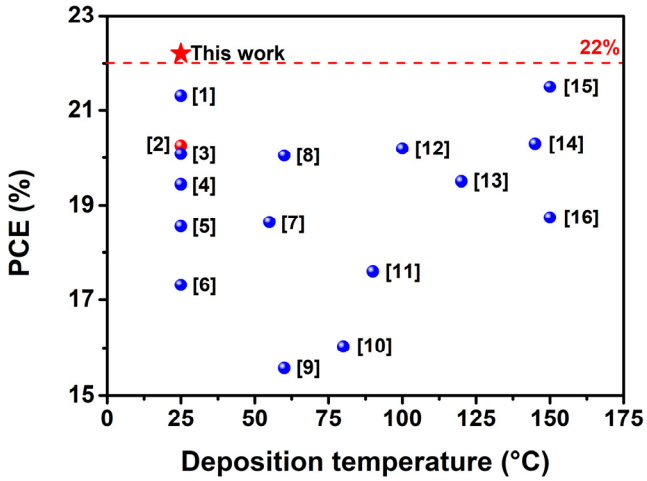

Figure S20. State-of-art PCEs versus deposition temperatures for the preparation of perovskite photovoltaic films though different scalable coating techniques summarized from the previous works.

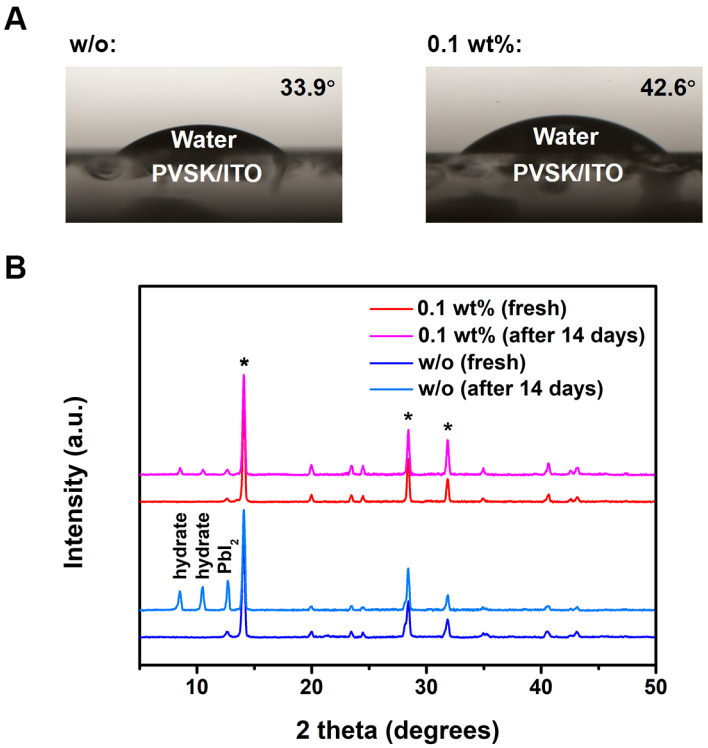

Figure S21. (A) Contact angles of the water droplet on the surface of pristine and TAH incorporated perovskite films. (B) Evolution of the perovskite phase for the pristine and TAH incorporated perovskite films exposed under 25 ± 5°C and 60 ± 10% RH for 14 days.

Table S1. Fitting parameters of the bi-exponential decay function in TRPL spectra of the perovskites with different amount of TAH.

TAH concentration (wt%)	A_1	τ_1 (ns)	A_2	τ_2 (ns)	Average decay time[a] τ (ns)
w/o	0.52	3.33	0.41	220.92	99.26
0.05	0.16	19.06	0.74	259.88	217.07
0.1	0.07	22.89	0.91	369.54	344.78

[a]Average decay time was calculated according to the equation: $\tau = (A_1\tau_1 + A_2\tau_2)/(A_1 + A_2)$.

Table S2. Fitting parameters of the bi-exponential decay function and initial PL intensity in fluence-dependent TRPL spectra of the TAH incorporated perovskite excited at 636.2 nm (0.1 to 4 nJ/cm^2).

Excitation fluence (nJ/cm^2)	A_1	τ_1 (ns)	A_2	τ_2 (ns)	Average decay time[a] τ (ns)	Initial PL intensity [t=0] (a.u.)
0.1	0.25	28.92	0.59	482.54	347.53	113
0.25	0.18	23.13	0.69	436.94	351.32	315
0.5	0.16	24.27	0.77	418.11	350.35	513
1	0.15	24.58	0.81	401.90	342.94	1070
2	0.11	23.02	0.84	381.92	340.36	2123
4	0.07	22.89	0.91	369.54	344.78	4222

[a]Average decay time was calculated according to the equation: $\tau = (A_1\tau_1 + A_2\tau_2)/(A_1 + A_2)$.

Table S3. Fitting parameters of the bi-exponential decay function in TRPL spectra of the TAH incorporated perovskite excited at 375.2 and 636.2 nm (4 nJ/cm^2) respectively.

Excitation wavelength (nm)	A_1	τ_1 (ns)	A_2	τ_2 (ns)	Average decay time[a] τ (ns)
375.2	0.55	4.58	0.47	267.43	125.70
636.2	0.07	22.89	0.91	369.54	344.78

[a]Average decay time was calculated according to the equation: $\tau = (A_1\tau_1 + A_2\tau_2)/(A_1 + A_2)$.

Table S4. Band structure of PTAA, pristine $MAPbI_3$, TAH based $MAPbI_3$, and $PC_{61}BM$.

Conditions	Bandgap (eV)	$E_{cut\text{-}off}$ (eV)	$E_{edge\text{-}on}$ (eV)	Work function (eV)	HOMO energy level (eV)	LUMO energy level[a] (eV)
PTAA	3.30	16.60	0.64	-4.62	-5.26	-1.96
Pristine $MAPbI_3$	1.59	16.52	1.21	-4.70	-5.91	-4.32
TAH based $MAPbI_3$	1.59	16.61	1.18	-4.61	-5.79	-4.20
$PC_{61}BM$	1.80	16.86	1.70	-4.36	-6.06	-4.26

[a]LUMO energy level was calculated from HOMO and optical bandgap.

Table S5. Photovoltaic parameters of the blade-coated PSCs in conventional n-i-p structure.

Conditions (active area)	V_{OC} (V)	J_{SC}[a] (mA cm^{-2})	FF (%)	PCE (%)	
				Average[b]	Best
w/o (0.04 cm^2)	1.175	23.28	74.06	19.60 ± 0.42	20.26
0.1 wt% TAH (0.04 cm^2)	1.205	23.68	77.79	21.46 ± 0.47	22.20
0.1 wt% TAH (0.8 cm^2)	1.186	23.45	75.59	19.88 ± 0.65	21.02

[a]AR MgF_2 films were deposited on the incident side of ITO/glass substrate.

[b]Average value and standard deviation were calculated from 10 devices.

Table S6. State-of-the-art PCEs of the upscaling coated PSCs under different deposition techniques and temperatures summarized from previous relevant works.

Reference	PCE (%)	Deposition temperature (°C)	Active area (cm^2)	Deposition technique
This work	22.20 21.02	25	0.04 0.8	Doctor blading
[1]	21.30 16.40	25	0.08 63.7	Doctor blading
[2]	20.26 18.76	25	0.06 1	Doctor blading
[3]	20.08 19.12	25	0.09 1	Air blading
[4]	19.44 13.85	25	0.12 16	Doctor blading
[5]	18.55 17.33	25	0.12 1.2	Doctor blading
[6]	17.31	25	0.15	Slot-die coating
[7]	18.64 17.74	55	0.04 2.02	Inkjet printing
[8]	20.05	60	0.1	Doctor blading
[9]	15.57	60	0.1	Slot-die coating
[10]	16.03 13.09	60-80	0.1 1	Ultrasonic spray
[11]	17.60	90	1	Soft-cover deposition
[12]	20.20	100	0.08	Doctor blading

[13]	19.50	120	NA	Doctor blading
[14]	20.30 15.30	145	0.075 33	Doctor blading
[15]	21.50 20.00	150	0.08 1.1	Doctor blading
[16]	18.74 17.06	150	0.09 1	Doctor blading

Note S1: GIWAXS distinguishes surface signal from bulk signal

Ex-situ GIWAXS measurement (Cu X-ray source, 8.05 keV, 1.54 Å) was carried out under two incident angles (α_i = 0.2° and 1° respectively). The penetration depth (Z_p) into perovskite (X-ray absorption coefficient ≈ 26 mm^{-1}) with α_i = 0.2° was calculated to be ~100 nm, and ~700 nm with α_i = 1°.[17] In the GIWAXS intensity profiles (Figure S11), neither the pristine nor the TAH based perovskites showed any diffraction signal of ITO (q = 2.15 $Å^{-1}$) with α_i = 0.2°. While, a 1° incident X-ray could penetrate the whole thickness of perovskite, and we detected the signal of ITO ((222) plane, q = 2.15 $Å^{-1}$) in both pristine and TAH based perovskite films. Therefore, this technique was reliable to distinguish the surface signal from bulk signal.[18]

Note S2: Initial density of photogenerated carrier and nonradiative recombination behaviors in TRPL

The initial density of photogenerated carriers (N_0) in TRPL when excited with a 636.2 nm picosecond pulsed diode laser (EPL-635, ~5 nJ/cm^2) was estimated using the following equation:[19]

$$N_0 = \frac{A(\lambda)\times F}{E_{\mathrm{ph}}(\lambda)\times W} \qquad \text{(Supplemental equation 1)}$$

in which F is the total incident fluence at excitation wavelength λ = 636.2 nm (~5 nJ/cm^2), photon energy $E_{ph}(\lambda)$ ≈ 3.12×10^{-10} nJ, perovskite film thickness W = 400 nm; $A(\lambda)$ is the overall absorbance, which can be estimated using the following equation:

$$A(\lambda) = 1 - R - T = \left(1 - e^{-\alpha(\lambda)\cdot W}\right)\cdot(1-\mathrm{R}) \qquad \text{(Supplemental equation 2)}$$

in which R and T are the reflectance and transmittance respectively, $\alpha(\lambda)$ is the absorption coefficient. For $MAPbI_3$ based perovskite, the overall absorbance was calculated to be A(636.2 nm) ≈ 0.92 with the α(636.2 nm) ≈ 5 × 10^4 cm^{-1}.[20] Therefore, N_0 can be calculated to be 2.4 × 10^{14} cm^{-3}, which is much lower than the density of trap states measured in TAS analysis.

Fluence-dependent TRPL decay for the sample of TAH incorporated perovskite film on quartz substrate was performed in order to reveal the PL lifetime and initial PL intensity right after the excitation of a 636.2 nm pulsed laser as a function of its fluence (Figure 3C and Figure S12B). The initial PL intensity exhibited a linear dependence on the excitation fluence, and the PL lifetime kept almost constant (summarized in Table S2), which confirmed low excitation fluence (≤ 5 nJ/cm^2) in TRPL mainly triggered the trapping and nonradiative recombination behaviors of photogenerated carriers.

We also performed wavelength-dependent TRPL decay with the excitation of a 375.2 nm (EPL-375) and a 636.2 nm (EPL-635) pulsed laser respectively, as shown in Figure S12C. Compared with the 636.2 nm laser ($Z_p = 1/\alpha$ ≈ 500 nm), the penetration depth (Z_p) of the 375.2 nm laser is much lower (~50 nm). Therefore, TRPL with the excitation at 375.2 nm mainly reflected the signal at perovskite upper surface. We compared the fitting parameters of the TAH incorporated perovskite under these two conditions (Table S3). The 375.2 nm excitation displayed much higher proportion of the fast decay (A_1 = 53.9%) compared with that at 636.2 nm (A_1 = 7.1%). This result further indicates the fast decay (τ_1) is likely relevant with surface recombination; while the slow decay (τ_2) originates from the deeper sub-surface region or in the bulk.[21]

Note S3: Temperature dependent admittance spectroscopy analysis

Thermal dependent admittance spectroscopy (TAS) is a well-established and effective technique to quantitatively characterize both shallow and deep defects, which has been widely applied for understanding defects in organic solar cells and PSCs. The defect activation energy (E_a) can be derived using the equation:

$$\omega_0 = \beta T^2 \exp\left(\frac{-E_a}{k_B T}\right) \quad \text{(Supplemental equation 3)}$$

in which ω_0 is characteristic transition (attempt to escape) angular frequency, β is a temperature independent parameter, k_B is Boltzmann constant, and T is temperature. The derivative of the capacitance spectra was used to define ω_0. According to this equation, the values of E_a and β were determined from the fitting slope in Arrhenius plot of the characteristic angular frequency.[22] The energetic profile of trap density of states (N_t) can be derived from the angular frequency dependent capacitance according to the equation:

$$N_t(E_\omega) = -\frac{V_{bi}}{eW}\frac{dC}{d\omega}\frac{\omega}{k_B T} \quad \text{(Supplemental equation 4)}$$

$$E_\omega = k_B T \ln\left(\frac{\beta T^2}{\omega}\right) \quad \text{(Supplemental equation 5)}$$

in which V_{bi} is the built-in potential, W is the depletion width, e is the elementary charge, C is the capacitance, and ω is the applied angular frequency. Mott-Schottky junction was obtained by capacitance-voltage measurement, which was analyzed to obtain V_{bi} and W.

Supplemental References:

[1] Deng, Y., Van Brackle, C.H., Dai, X., Zhao, J., Chen, B., and Huang, J. (2019). Tailoring solvent coordination for high-speed, room-temperature blading of perovskite photovoltaic films. Sci. Adv. *5*, eaax7537.

[2] Hu, H., Ren, Z., Fong, P.W.K., Qin, M., Liu, D., Lei, D., Lu, X., and Li, G. (2019). Room‐temperature meniscus coating of >20% perovskite solar cells: a film formation mechanism investigation. Adv. Funct. Mater. *29*, 1900092.

[3] Ding, J., Han, Q., Ge, Q.-Q., Xue, D.-J., Ma, J.-Y., Zhao, B.-Y., Chen, Y.-X., Liu, J., Mitzi, D.B., and Hu, J.-S. (2019). Fully air-bladed high-efficiency perovskite photovoltaics. Joule *3*, 402-416.

[4] Lee, D.-K., Jeong, D.-N., Ahn, T.K., and Park, N.-G. (2019). Precursor engineering for a large-area perovskite solar cell with >19% efficiency. ACS Energy Letters *4*, 2393-2401.

[5] Yang, M., Li, Z., Reese, M.O., Reid, O.G., Kim, D.H., Siol, S., Klein, T.R., Yan, Y., Berry, J.J., van Hest, M.F.A.M., et al. (2017). Perovskite ink with wide processing window for scalable high-efficiency solar cells. Nat. Energy *2*. 17038.

[6] Dou, B., Whitaker, J.B., Bruening, K., Moore, D.T., Wheeler, L.M., Ryter, J., Breslin, N.J., Berry, J.J., Garner, S.M., Barnes, F.S., et al. (2018). Roll-to-roll printing of perovskite solar cells. ACS Energy Lett. *3*, 2558-2565.

[7] Li, P., Liang, C., Bao, B., Li, Y., Hu, X., Wang, Y., Zhang, Y., Li, F., Shao, G., and Song, Y. (2018). Inkjet manipulated homogeneous large size perovskite grains for efficient and large-area perovskite solar cells. Nano Energy *46*, 203-211.

[8] He, M., Li, B., Cui, X., Jiang, B., He, Y., Chen, Y., O'Neil, D., Szymanski, P., Ei-Sayed, M.A., Huang, J., et al. (2017). Meniscus-assisted solution printing of large-grained perovskite films for high-efficiency solar cells. Nat. Commun. *8*, 16045.

[9] Zuo, C., Vak, D., Angmo, D., Ding, L., and Gao, M. (2018). One-step roll-to-roll air processed high efficiency perovskite solar cells. Nano Energy *46*, 185-192.

[10] Huang, H., Shi, J., Zhu, L., Li, D., Luo, Y., and Meng, Q. (2016). Two-step ultrasonic spray deposition of $CH_3NH_3PbI_3$ for efficient and large-area perovskite solar cell. Nano Energy *27*, 352-358.

[11] Ye, F., Chen, H., Xie, F., Tang, W., Yin, M., He, J., Bi, E., Wang, Y., Yang, X., and Han, L. (2016). Soft-cover deposition of scaling-up uniform perovskite thin films for high cost-performance solar cells. Energy Environ. Sci. *9*, 2295-2301.

[12] Wu, W.-Q., Wang, Q., Fang, Y., Shao, Y., Tang, S., Deng, Y., Lu, H., Liu, Y., Li, T., Yang, Z., et al. (2018). Molecular doping enabled scalable blading of efficient hole-transport-layer-free perovskite solar cells. Nat. Commun. *9*, 1625.

[13] Tang, S., Deng, Y., Zheng, X., Bai, Y., Fang, Y., Dong, Q., Wei, H., and Huang, J. (2017). Composition engineering in doctor-blading of perovskite solar cells. Adv. Energy Mater. *7*, 1700302.

[14] Deng, Y., Zheng, X., Bai, Y., Wang, Q., Zhao, J., and Huang, J. (2018). Surfactant-controlled ink drying enables high-speed deposition of perovskite films for efficient photovoltaic modules. Nat. Energy *3*, 560-566.

[15] Wu, W.-Q., Yang, Z., Rudd, P.N., Shao, Y., Dai, X., Wei, H., Zhao, J., Fang, Y., Wang, Q., Liu, Y., et al. (2019). Bilateral alkylamine for suppressing charge recombination and improving stability in blade-coated perovskite solar cells. Sci. Adv. *5*, 8925.

[16] Li, J., Munir, R., Fan, Y., Niu, T., Liu, Y., Zhong, Y., Yang, Z., Tian, Y., Liu, B., Sun, J., et al. (2018). Phase transition control for high-performance blade-coated perovskite solar cells. Joule *2*, 1313-1330.

[17] Birkholz, M. (2006). Thin film analysis by X-ray scattering. John Wiley & Sons.

[18] Dong, J., Shao, S., Kahmann, S., Rommens, A.J., Hermida‐Merino, D., ten Brink, G.H., Loi, M.A., and Portale, G. (2020). Mechanism of crystal formation in ruddlesden–popper Sn‐Based Perovskites. Adv. Funct. Mater. 30, 2001294.

[19] Yang, J., Wen, X., Xia, H., Sheng, R., Ma, Q., Kim, J., Tapping, P., Harada, T., Kee, T.W., Huang, F., et al. (2017). Acoustic-optical phonon up-conversion and hot-phonon bottleneck in lead-halide perovskites. Nat. Commun. *8*, 14120.
[20] Song, T.-B., Chen, Q., Zhou, H., Jiang, C., Wang, H.-H., Yang, Y., Liu, Y., You, J., and Yang, Y. (2015). Perovskite solar cells: film formation and properties. J. Mater. Chem. A *3*, 9032-9050.
[21] Wu, B., Nguyen, H.T., Ku, Z., Han, G., Giovanni, D., Mathews, N., Fan, H.J., and Sum, T.C. (2016). Discerning the surface and bulk recombination kinetics of organic-inorganic halide perovskite single crystals. Adv. Energy Mater. *6*, 1600551.
[22] Meng, X., Ho, C.H.Y., Xiao, S., Bai, Y., Zhang, T., Hu, C., Lin, H., Yang, Y., So, S.K., and Yang, S. (2018). Molecular design enabled reduction of interface trap density affords highly efficient and stable perovskite solar cells with over 83% fill factor. Nano Energy *52*, 300-306.